FTIR time series of tropospheric HCN in eastern China: seasonality, interannual variability and source attribution

Youwen Sun [1)], Cheng Liu [1, 2, 3, 4, 5)*], Lin Zhang [6)*], Mathias Palm [7)], Justus Notholt [7)], Hao Yin [1)], Corinne Vigouroux [8)], Erik Lutsch [9)], Wei Wang [1)], Changong Shan [1)], Thomas Blumenstock [10)], Tomoo Nagahama [11)], Isamu Morino [12)], Emmanuel Mahieu [13)], Kimberly Strong [9)], Bavo Langerock [8)], Martine De Maziere [8)], Qihou Hu [1)], Huifang Zhang [1)], Christoph Petri [7)], and Jianguo Liu [1)]

(1 *Key Laboratory of Environmental Optics and Technology, Anhui Institute of Optics and Fine Mechanics, Chinese Academy of Sciences, Hefei 230031, China*)

(2 *Center for Excellence in Regional Atmospheric Environment, Institute of Urban Environment, Chinese Academy of Sciences, Xiamen, 361021, China*)

(3 *University of Science and Technology of China, Hefei, 230026, China*)

(4 *Key Laboratory of Precision Scientific Instrumentation of Anhui Higher Education Institutes, University of Science and Technology of China*)

(5 *Anhui Province Key Laboratory of Polar Environment and Global Change, USTC, Hefei, 230026, China*)

(6 *Laboratory for Climate and Ocean–Atmosphere Studies, Department of Atmospheric and Oceanic Sciences, School of Physics, Peking University, Beijing 100871, China*)

(7 *University of Bremen, Institute of Environmental Physics, P. O. Box 330440, 28334 Bremen, Germany*)

(8 *Royal Belgian Institute for Space Aeronomy (BIRA-IASB), Brussels, Belgium*)

(9 *Department of Physics, University of Toronto, Toronto, Ontario, Canada*)

(10 *Karlsruhe Institute of Technology (KIT), Institute for Meteorology and Climate Research (IMK-ASF), Karlsruhe, Germany*)

(11 *Institute for Space-Earth Environmental Research (ISEE),Nagoya University, Nagoya, 464-8601, Japan)*

(12 *Satellite Observation Center, National Institute for Environmental Studies, Tsukuba, 305-8506, Japan*)

(13 *Institute of Astrophysics and Geophysics, University of Liège, Belgium*)

Correspondence: Cheng Liu (chliu81@ustc.edu.cn) or Lin Zhang (zhanglg@pku.edu.cn)

Abstract:

We analyzed seasonality and interannual variability of tropospheric HCN columns in densely populated eastern China for the first time. The results were derived from solar absorption spectra recorded with ground-based high spectral resolution Fourier transform infrared (FTIR) spectrometer at Hefei (117°10′E, 31°54′N) between 2015 and 2018. The tropospheric HCN columns over Hefei, China showed significant seasonal variations with three monthly mean peaks throughout the year. The magnitude of the tropospheric HCN column peak in May > September > December. The tropospheric HCN column reached a maximum monthly mean of $(9.8 \pm 0.78) \times 10^{15}$ molecules/cm^2 in May and a minimum monthly mean of $(7.16 \pm 0.75) \times 10^{15}$ molecules/cm^2 in November. In most cases, the tropospheric HCN columns at Hefei (32°N) are higher than the FTIR observations at Ny Alesund (79°N), Kiruna (68°N), Bremen (53°N), Jungfraujoch (47°N), Toronto (44°N), Rikubetsu (43°N), Izana (28°N), Mauna Loa (20°N), La Reunion Maido (21°S), Lauder (45°S), and Arrival Heights (78°S) that are affiliated with the Network for Detection of Atmospheric Composition Change (NDACC). Enhancements of tropospheric HCN column were observed between September 2015 and July 2016 compared to the same period of measurements in other years. The magnitude of the enhancement ranges from 5 to 46% with an average of 22%. Enhancement of tropospheric HCN (ΔHCN) is correlated with the concurrent enhancement of tropospheric CO (ΔCO), indicating that enhancements of tropospheric CO and HCN were due to the same sources. The GEOS-Chem tagged CO simulation, the global fire maps and the Potential Source Contribution Function values

(PSCFs) calculated using back trajectories revealed that the seasonal maxima in May is largely due to the influence of biomass burning in South Eastern Asia (SEAS) (41 ± 13.1%), Europe and Boreal Asia (EUBA) (21 ± 9.3%) and Africa (AF) (22 ± 4.7%). The seasonal maxima in September is largely due to the influence of biomass burnings in EUBA (38 ± 11.3%), AF (26 ± 6.7%), SEAS (14 ± 3.3%), and Northern America (NA) (13.8 ± 8.4%). For the seasonal maxima in December, dominant contributions are from AF (36 ± 7.1%), EUBA (21 ± 5.2%), and NA (18.7 ± 5.2%).The tropospheric HCN enhancement between September 2015 and July 2016 at Hefei (32°N) were attributed to an elevated influence of biomass burnings in SEAS, EUBA, and Oceania (OCE) in this period. In particular, an elevated fire number in OCE in the second half of 2015 dominated the tropospheric HCN enhancement in September – December 2015. An elevated fire number in SEAS in the first half of 2016 dominated the tropospheric HCN enhancement in January – July 2016.

1 Introduction

Atmospheric hydrogen cyanide (HCN) is an extremely hazardous gas that threaten human health and terrestrial ecosystems (Andreae and Merlet, 2001; Akagi et al., 2011; Rinsland et al., 2002). Improved knowledge of the physical and chemical mechanisms which drive the observed HCN variability is of great significance because HCN plays an important role in the global nitrogen cycle (Andreae and Merlet, 2001; Li et al., 2003). It is well established that biomass burning is the major source of tropospheric HCN and industrial emissions contribute additional minor sources of HCN (Bange and Williams, 2000; Holzinger et al., 1999; Lobert et al., 1990). Li et al. (2009) estimates a global source of HCN from biomass burning of 0.4 – 3.2 Tg N yr^{-1} and from burning domestic biofuel of 0.2 Tg N yr^{-1} (Li et al., 2009). Bertschi et al. (2003) estimates a global fossil fuel combustion source of 0.04 Tg N yr^{-1}, negligibly small in comparison (Bertschi et al., 2003). The principle pathway for HCN sink is ocean uptake which accounts for 0.73 to 1.0 Tg N/year (Li et al., 2009). Additional minor sinks of HCN are attributed to atmospheric reaction with hydroxyl radical (OH) and $O(^1D)$, and photolysis (Li et al., 2000; Nagahama and Suzuki, 2007). The life time of HCN is 2 – 5 months in the troposphere and several years in the stratosphere. Li et al. (2003, 2009), Lupu et al. (2009), Vigouroux et al. (2012), and Zeng et al. (2012) showed that the observed variability of HCN can be reproduced by the chemical model simulations where biomass burning and ocean uptake provide the main source and sink, respectively (Li et al., 2009; Li et al., 2003; Lupu et al., 2009; Vigouroux et al., 2012; Zeng et al., 2012).

With the rapid economic growth in China over the past three decades, the anthropogenic emissions have increased dramatically, raising concerns about worsening air quality in China (Tang et al., 2012; Chan, 2017; Xing et al., 2017; Wang et al., 2017). These emissions are from automobile exhaust, industrial processes and biomass burning. Many researchers have evaluated regional emissions in various pollution regions (e.g., the Jing-Jin-Ji region, the Yangtze River Delta region, and the Pearl River Delta region, Fig. S1), but the relative contribution of the biomass burning, automobile exhaust, and industrial processes is seldom mentioned in the literature (Tang et al., 2012; Chan, 2017; Wang et al., 2017; Sun et al., 2018a; Xing et al., 2017). This is because both industrial emissions and biomass burning are major sources of the trace gases (e.g. carbon monoxide (CO), formaldehyde (HCHO) and carbon dioxide (CO_2)) that were used to evaluate regional emissions in the literature, and it is hard to quantify their relative contribution under the complex pollution condition in China (Chan et al., 2018; Tang et al., 2012; Wang et al., 2017; Xiaoyan et al., 2010; Xing et al., 2017). It has been proved that HCN is an unambiguous tracer of biomass burning emission due to its inactive chemical feature and long lifetime (Rinsland et al., 2002; Zhao et al., 2002). Therefore, measurements of HCN made in the polluted troposphere over eastern China at middle latitudes are particularly useful in determining the potential biomass burning sources that drive the observed tropospheric HCN seasonality and interannual variability in China.

Ground based high-resolution Fourier Transform Spectroscopy (FTIR) measurements of trace gases made by Anhui Institute of Optics and Fine Mechanics, Chinese Academy of Sciences (AIOFM-CAS) at Hefei (117°10′E, 31°54′N, 30 m a.s.l. (above sea level)) is one of few multiyear time series of trace gases on Asian continent (Sun et al., 2018a; Sun et al., 2018b). These measurements are crucial to understanding global warming, regional pollution, and long term transport. Both HCN and CO are regularly measured at Hefei (32°N) using the FTIR observations, where influences from biomass burning occurring at long distances or locally can be assessed.

In this study, we analyze the first multiyear measurements of tropospheric HCN in densely populated eastern China. In section 2 the retrieval strategy to derive HCN from high resolution FTIR

spectrometry and the methods for a GEOS-Chem tagged CO simulation and potential source contribution function (PSCF) calculation are summarized. In section 3 we present the seasonal and interannual variability of tropospheric HCN columns measured at Hefei (32° N), China and comparisons with the measurements affiliated with Network for Detection of Atmospheric Composition Change (NDACC, http://www.ndacc.org/, last accessed on 3 June 2019). The potential sources that drive the observed HCN variability are determined by using the GEOS-Chem tagged CO simulation, the global fire maps and the PSCFs analysis in section 4. The work concludes with a summary in section 5. This study aims to improve our understanding of regional biomass burning characteristic and transport, and contribute to the evaluation of the global nitrogen cycle.

2 Methods

2 FTIR observations

2.1.1 Site description and instrumentation

The routine observations of atmospheric trace gases using ground based high-resolution FTIR spectrometer at Hefei (117°10′E, 31°54′N, 30 m a.s.l.) started in July 2014. Location of Hefei site alongside those of the NDACC FTIR stations selected for comparison are shown in Fig.1. Geographical source regions used in the standard GEOS-Chem tagged CO simulation are also marked in Fig.1. Detailed description of Hefei site can be found in Tian et al., 2017. We follow the NDACC requirements, and plan to apply for acceptance within the NDACC in the future.

A Bruker IFS 125 HR with maximum optical path difference (OPD) of 900 cm is used to take the solar spectra (Tian et al., 2017). Defined as 0.9/OPD, this instrument can reach the highest spectral resolution of 0.001 cm^{-1}. However, all mid-infrared (MIR) spectra are recorded with a spectral resolution of 0.005 cm^{-1} to follow NDACC convention. This spectral resolution is sufficient to resolve the optical absorption structure of all gases in the atmosphere. The FTIR spectrometer covered a wide spectral range (about 600 – 4500 cm^{-1}) but, depending on the species, specific detectors and band-pass filters are applied (Sun et al. 2018a). In this study, the instrument is equipped with a KBr beam splitter, an InSb detector, and a filter centered at 2900 cm^{-1} for HCN measurements, and a KBr beam splitter, an InSb detector, and a filter centered at 2400 cm^{-1} for CO measurements. The entrance field stop size ranging from 0.80 to 1.5 mm was employed to maximise the signal to noise ratio (SNR) consistent with the maximum frequency possible for the selected wavenumber range. The number of measurements within a day varies from 1 to 20. In total, there were 651 and 649 days of qualified measurements between 2015 and 2018 for CO and HCN, respectively.

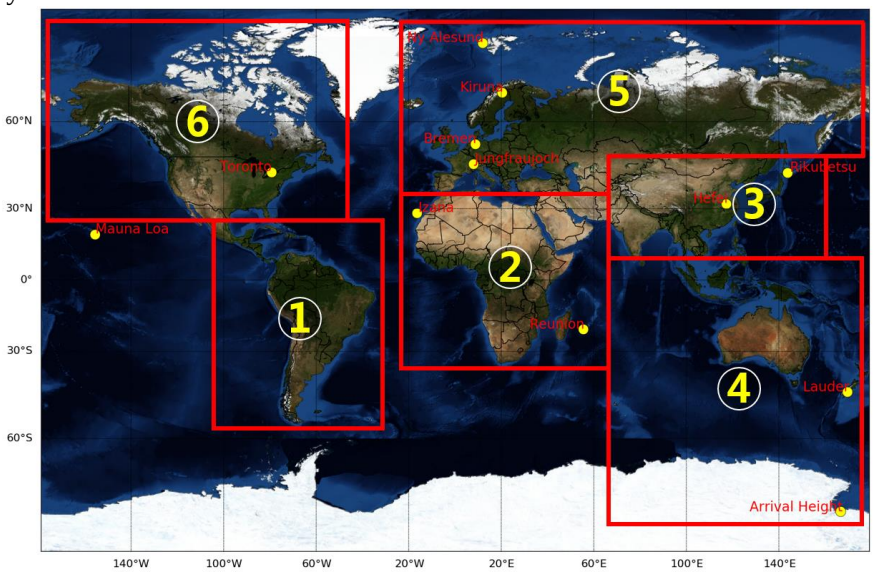

Fig. 1 Location of Hefei site alongside those of the NDACC FTIR stations (yellow dots) that are selected for comparison. Geographical source regions used in the standard GEOS-Chem tagged CO simulation are also shown. See Table 3 for latitude and longitude definitions

2.1.2 Retrieval strategy

The SFIT4 (version 0.9.4.4) algorithm is used to retrieve the vertical profiles of CO and HCN (Viatte et al., 2014). Both CO and HCN are standard NDACC species, and we follow the NDACC recommendation for micro windows (MWs) selection and the interfering gases consideration

(http://www.ndaccdemo.org/, last accessed on 23 May 2019). The retrieval inputs for CO and HCN are summarized in Table 1. Time series of tropospheric CO columns between 2014 and 2017 at Hefei (32°N) measured from the FTIR have been reported in Sun et al. (2018a) and the detailed description of CO profile retrieval can be found therein. Time series of tropospheric HCN columns at Hefei (32°N) are presented for the first time. Temperature and pressure profiles are extracted from National Centers for Environmental Protection (NCEP) 6-hourly reanalysis data (De Maziere et al., 2018) and all spectroscopic absorption parameters are prescribed from HITRAN 2008 database (Rothman et al., 2009). The water vapor (H_2O) *a priori* profile is interpolated from the NCEP 6-hourly reanalysis data and a priori profiles of other gases are from the Whole-Atmosphere Community Climate Model (WACCM) v6 special run for NDACC.

Three MWs were used for CO: a strong line at 2057.7–2058 cm^{-1} and two weak lines at 2069.56–2069.76 cm^{-1} and 2157.5–2159.15 cm^{-1} (Sun et al., 2018a). For HCN, two MWs were used: 3268.00 – 3268.38 cm^{-1} and 3287.00 – 3287.48 cm^{-1} (Mahieu et al., 1997; Lutsch et al., 2016; Notholt et al., 2000). In order to minimize the cross absorption interference, profiles of ozone (O_3) and nitrous oxide (N_2O) and columns of H_2O, carbonyl sulfide (OCS) and CO_2 are simultaneously retrieved in addition to the CO profile. Profile of H_2O and columns of O_3, C_2H_2, and CH_4 are simultaneously retrieved in addition to the HCN profile. No de-weighting SNR is used for HCN and a de-weighting SNR of 500 is used in the three MWs for CO.

The diagonal elements of *a priori* profile covariance matrices $\mathbf{S}_a$ are set to standard deviation of the WACCM v6 special run for NDACC, and its non-diagonal elements are set to zero. The diagonal elements of the measurement noise covariance matrices $\mathbf{S}_\varepsilon$ are set to the inverse square of the SNR calculated from each individual spectrum and its non-diagonal elements are set to zero. The measured instrument line shape (ILS) is included in the retrieval (Hase, 2012; Sun et al., 2018a).

Table 1. Retrieval inputs used for CO and HCN.

Gases	CO	HCN
Code	SFIT4 v 0.9.4.4	SFIT4 v 0.9.4.4
Spectroscopic parameters	HITRAN 2008	HITRAN 2008
P, T, H_2O profiles	NCEP reanalysis data	NCEP reanalysis data
A priori profiles of all gases except H_2O	WACCM v6	WACCM v6
Micro windows for profile retrievals (cm^{-1})	2057.7 – 2058 2069.56–2069.76 2157.5–2159.15	3268.00 – 3268.38 3287.00–3287.48
Retrieved interfering gases	O_3, N_2O, CO_2, OCS, H_2O	H_2O, O_3, C_2H_2, CH_4
SNR for de-weighting	500	None
$\mathbf{S}_a$	WACCM v6 standard deviation	WACCM v6 standard deviation
$\mathbf{S}_\varepsilon$	SNR calculated from each individual spectrum within 2526.23 – 2526.62	SNR calculated from each individual spectrum within 3381.16 – 3381.54
ILS	LINEFIT145 analysis	LINEFIT145 analysis
Error analysis	Systematic error: line intensity, line pressure broadening, line temperature broadening, solar zenith angle, background curvature, solar line strength, optical path difference, field of view, phase	
	Random error: -Measurement error -Smoothing error -Interference errors: interfering species, retrieval parameters - Other errors: zero level, temperature	

2.1.3 Averaging kernels and error budget

The partial column averaging kernels of CO and HCN at selected layers are shown in Fig. 2. The CO averaging kernels have three maxima at the surface, 7 km, and 14 km, respectively. The HCN averaging kernels only have one maxima at 10 km. Both CO and HCN retrievals show good vertical sensitivity in the whole troposphere where CO exhibits the best sensitivity with two maxima in the troposphere (Sun et al., 2018a). We can see in Table 2, the typical degrees of freedom (DOFS) obtained at Hefei (32°N) over the total atmosphere for CO and HCN are about 2.8 ± 0.3 (1σ) and 1.3 ± 0.2 (1σ), respectively. In this study, only partial columns of CO and HCN within a broad layer between surface and 15 km are considered. The selected layer corresponds roughly to the total troposphere over eastern China, as the mean tropopause height calculated from NCEP reanalysis data is around 15 km over four seasons. The selected layer corresponds to 2.3 ± 0.2 (1σ) and 1.0 ± 0.1 (1σ) of DOFS for CO and HCN, respectively.

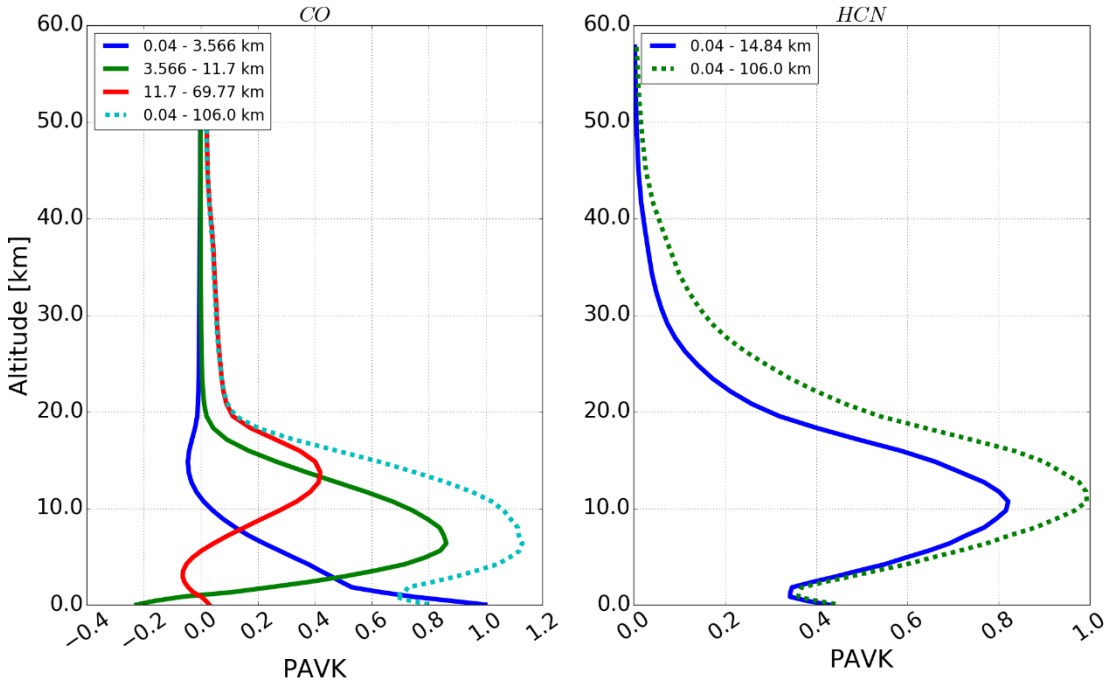

Fig. 2 Partial column averaging kernels (PAVKs) (ppmv / ppmv) for CO and HCN retrievals.

We calculated the error budget following the formalism of Rodgers, 2000, and separated all error items into systematic error or random error depending on whether they are constant over consecutive measurements, or vary randomly. Table 2 summarizes the random, the systematic, and the combined error budget of tropospheric CO and HCN columns. The error items included in the error budget are listed in Table 1. For CO, the major systematic error is line intensity uncertainty, and the major random error are zero level uncertainty and temperature uncertainty. For HCN, the major systematic error are line intensity uncertainty and line pressure broadening uncertainty, the major random error are smoothing error and measurement error. Total retrieval errors for tropospheric CO and HCN columns between surface and 15 km are estimated to be 8.3 and 14.2%, respectively.

Table 2. Retrieval error budgets and DOFs for tropospheric CO and HCN.

Gases	CO	HCN
Temperature uncertainty	2.5%	0.2%
Zero level uncertainty	5.2%	1.5%
Retrieval parameters uncertainty	< 0.1%	2.0%
Interfering species uncertainty	< 0.1%	1.3%
Measurement Error	< 0.1%	6.8%
Smooth Error	0.1%	11.0%
Total Random Error	5.7%	13.2%
Background curvature uncertainty	< 0.1%	*
Optical path difference uncertainty	< 0.1%	< 0.1%
Field of view uncertainty	< 0.1%	< 0.1%
Solar line strength uncertainty	< 0.1%	< 0.1%
Phase uncertainty	*	< 0.1%
Solar zenith angle uncertainty	0.1%	< 0.1%
Line temperature broadening uncertainty	0.13%	0.3%
Line pressure broadening uncertainty	0.87%	3.5%
Line intensity uncertainty	6.0%	3.7%
Total Systematic Error	6.1%	5.1%
Total Errors	8.3%	14.2%
DOFS (-)	2.2	1.0

* Not included into error budget since they are retrieved together with the target gas

2.2 GEOS-Chem tagged simulation

To interpret the influence of biomass burning sources on HCN columns at Hefei (32°N), the GEOS-Chem chemical transport model is used (http://geos-chem.org/; Bey et al., 2001b) in a tagged simulation of CO at a horizontal resolution of 2°×2.5° with 47 vertical hybrid levels. GEOS-Chem version 12.2.1 was used and driven by the Goddard Earth Observing System-Forward Processing

product (GEOS-FP) assimilated meteorological data observations from the NASA Global Modeling and Assimilation Office (GMAO). For driving the GEOS-Chem model, the GEOS-FP meteorological data with a native horizontal resolution of 0.25° latitude × 0.3125° longitude were downgraded to 2° latitude × 2.5° longitude and a vertical resolution of 72 hybrid levels (extending from surface to 0.01 hPa). The temporal resolution of surface variables and boundary layer height are 1hr and other variables are 3 hr.

The GEOS-Chem simulation was initialized with a 1-year spin-up from July 2014 to July 2015. Chemical and transport operator time-steps of 1 hr and 10 min, respectively, were used. Biomass burning emissions are from Global Fire Assimilation System (GFAS) v1.2 (Kaiser et al., 2012; Giuseppe et al., 2018; Erik et al, 2019) which assimilates Moderate Resolution Imaging Spectroradiomter (MODIS) burned area and fire radiative power (FRP) products to estimate emissions for open fires. GFASv1.2 emissions have a 0.1◦×0.1◦ horizontal resolution with 3-hourly temporal resolution. GFAS was chosen for the availability of emissions over the analysis period of 2015 - 2018. Global anthropogenic and biofuel emissions are from the Community Emissions Data System (CEDS) inventory (Hoesly et al., 2018). In particular, the latest Multi-resolution Emission Inventory for China (MEIC) is used to provide Chinese anthropogenic emissions (Li et al., 2017). Biogenic emissions of precursor VOCs are from the Model of Emissions of Gases and Aerosols from Nature (MEGANv2.1; Guenther et al., 2012) and biofuel emissions are taken from Yevich and Logan (2003). The main loss mechanism for CO is from photochemical oxidation by the hydroxyl radical (OH). The OH fields were obtained from monthly mean OH concentrations archived from a previous full-chemistry simulation. Surface emissions in GEOS-Chem are released within the boundary layer, and boundary layer mixing is implemented using the non-local mixing scheme of Holtslag and Boville (1993). Biomass emissions are released by uniformly distributing emissions from the surface to the mean altitude of maximum injection based on the injection height information as described in Rémy et al. (2017) which includes an injection height parameterization by Sofiev et al. (2012) and a plume rise model by Freitas et al. (2007).

GEOS-Chem version 12.2.1 tagged CO simulation includes the improved secondary CO production scheme of Fisher et al. (2017), which assumes production rates of CO from CH_4 and NMVOC (non-methane volatile organic compounds) oxidation from a GEOS-Chem full-chemistry simulation therefore reducing the mismatch between the CO-only simulation and the full-chemistry simulation.

The tracers of anthropogenic, biomass burning, CH_4 and NMVOC oxidations are implemented following the standard GEOS-Chem tagged CO simulation (Giglio et al., 2013). In this study, we only investigate the influence from the biomass burning sources. The regional definition of all biomass burning tracers are shown in Fig. 1 and tabulated in Table 3.

Table 3. Regional definitions of all biomass burning tracers implemented in the standard GEOS-Chem tagged CO simulation

No.	Tracer	Description	Region
1	SA	Biomass burning CO emitted over South America	112.5°W - 32.5°W; 56°S - 24°N
2	AF	Biomass burning CO emitted over Africa	17.5°W -70.0°E; 48.0°S - 36.0°N
3	SEAS	Biomass burning CO emitted over Southeast Asia	70.0°E - 152.5°E; 8.0°N - 45.0°N
4	OCE	Biomass burning CO emitted over Oceania	70.0°E - 170.0°E; 90.0°S - 8.0°N
5	EUBA	Biomass burning CO emitted over Europe and Boreal Asia	17.5°W - 72.5°E; 36.0°N - 45.0°N and 17.5°W - 172.5°E; 45.0°N - 88.0°N
6	NA	Biomass burning CO emitted over North America	173°W - 50°W; 24.0°N - 88.0°N

2.3 Potential source contribution function

We used the potential source contribution function (PSCF) analysis method to identify air masses associated with high levels of air pollutants. The PSCF assumes that back trajectories arriving at times of higher concentrations likely point to the more significant pollution directions (Ashbaugh et al., 1985). PSCF has been applied in many studies to locate air masses associated with high levels of air pollutants (Kaiser et al., 2007; Dimitriou and Kassomenos, 2015; Yin et al., 2017). In this study, PSCF values were calculated using back trajectories that were calculated by HYSPLIT.

The top of the model was set to 10 km. The PSCF values for the grid cells in the study domain were based on a count of the trajectory segment that terminated within each cell (Ashbaugh et al., 1985). The number of endpoints that fall in the ij^{th} cell is designated n_{ij}. The number of endpoints for the same cell having arrival times at the sampling site corresponding to concentrations higher than an arbitrarily set criterion is defined to be m_{ij}. In this study, we calculated the PSCF values based on trajectories corresponding to concentrations that exceeded the monthly mean level of tropospheric HCN column during measurement. The PSCF value for the ij^{th} cell is then defined as:

$$PSCF_{ij} = m_{ij}/n_{ij} \quad (1)$$

The PSCF value can be interpreted as the conditional probability that the concentrations of a given analyte greater than the criterion level are related to the passage of air parcels through the ij^{th} cell during transport to the receptor site. That is, cells with high PSCF values are associated with the arrival of air parcels at the receptor site that have concentrations of the analyte higher than the criterion value. These cells are indicative of areas of 'high potential' contributions for the constituent.

Identical $PSCF_{ij}$ values can be obtained from cells with very different counts of back-trajectory points (e.g., grid cell A with m_{ij} = 400 and n_{ij} = 800 and grid cell B with m_{ij} = 4 and n_{ij} = 8). In this extreme situation grid cell A has 100 times more air parcels passing through than grid cell B. Because of the sparse particle count in grid cell B, the PSCF values are more uncertain. To account for the uncertainty due to low values of n_{ij}, the PSCF values were scaled by a weighting function W_{ij} (Polissar et al., 1999). The weighting function reduced the PSCF values when the total number of endpoints in a cell was less than approximately 3 times the average value of the end points per cell. In this case, W_{ij} was set as follows:

$$W_{ij} = \begin{cases} 1.00 & n_{ij} > 3N_{ave} \\ 0.70 & 3N_{ave} > n_{ij} > 1.5N_{ave} \\ 0.42 & 1.5\,N_{ave} > n_{ij} > N_{ave} \\ 0.05 & N_{ave} > n_{ij} \end{cases} \quad (2)$$

where *Nave* represents the mean n_{ij} of all grid cells. The weighted PSCF values were obtained by multiplying the original PSCF values by the weighting factor.

3 FTIR time series and comparisons with NDACC counterparts

The new HCN data are compared with the concurrent measurements regularly measured at eleven NDACC stations to investigate the representativeness of the observation site at Hefei (32°N) in polluted eastern China. These NDACC stations cover over a wide latitude range from 77.8°S to 78.9°N and a wide longitude range from 79°W to 170°E (http://www.ndaccdemo.org/, last access on 19 July 2019). Most of these NDACC stations use the same instrument and retrieval algorithm as those of Hefei (32°N). Alternatively, the high resolution spectrometers Bruker 125M, 120HR, or Bomem DA8 and the retrieval algorithm PROFFIT are used in other stations. It has been demonstrated that the profiles derived from these different instruments and algorithms are in excellent agreement (Hase et al., 2004; De Maziere et al., 2018). In addition, we show the time series of tropospheric CO columns, also measured with FTIR spectrometer, because we will discuss the correlation between HCN and CO, and quantify the influence of biomass burning sources on HCN columns at Hefei (32°N) by using a tagged CO simulation. The upper limit of 15 km is above the tropopause at most of the NDACC stations. For most NDACC stations, the surface – 15 km layer is a mixture of troposphere and a part of stratosphere. However, we did not find major changes in the results of this study when choosing a lower upper limit such as 12 km. Thus we have chosen the same upper limits for all stations. The geolocations of all FTIR stations and their seasonal maximum, minimum and variabilities are summarized in Table 4.

Table 4. Tropospheric HCN and CO columns at Hefei (32°N), China from 2015 to 2018 alongside those of the NDACC FTIR stations. All stations are organised as a function of decreasing latitude.

Station	Location (Lon., Lat., Alt. in km)	Instrument	Algorithm	Maximum (molecules cm^{-2})		Minimum (molecules cm^{-2})	
				HCN (10^{15})	CO (10^{18})	HCN (10^{15})	CO (10^{18})
Ny Alesund	(12°E, 79°N, 0.02)	125HR	SFIT4	5.94± 1.20 (August)	2.11 ± 0.11 (March)	3.75 ± 0.37 (March)	1.56 ± 0.12 (July)
Kiruna	(20°E, 68°N, 0.42)	125HR	PROFFIT	5.81 ± 0.58 (August)	2.1 ± 0.01 (January)	2.43 ± 0.27 (January)	1.45 ± 0.09 (July)
Bremen	(9°E, 53°N, 0.03)	125HR	SFIT4	6.11 ± 0.87 (August)	2.32 ± 0.13 (March)	2.85 ± 0.25 (January)	1.63 ± 0.19 (July)
Jungfraujoch	(8°E, 46.5°N, 3.58)	125HR	SFIT4	4.68 ± 0.63 (May)	1.14 ± 0.08 (March)	2.1 ± 0.29 (February)	0.88 ± 0.08 (July)

Toronto	(79°W, 44°N, 0.17)	Bomem DA8	SFIT4	5.92 ± 1.13 (May)	2.19 ± 0.15 (April)	3.12 ± 1.02 (November)	1.74 ± 0.1 (October)
Rikubetsu	(144°E, 43°N, 0.38)	125HR	SFIT4	7.0 ± 1.92 (May)	2.32 ± 0.31 (March)	2.86 ± 0.44 (February)	1.79 ± 0.14 (October)
Hefei	**(117°E, 32°N, 0.03)**	**125HR**	**SFIT4**	**9.8 ± 0.78 (May)**	**3.38 ± 0.43 (February)**	**7.16 ± 0.75 (November)**	**2.29 ± 0.48 (July)**
Izana	(16°W, 28°N, 2.37)	125HR	PROFFIT	5.33 ± 1.2 (May)	1.41 ± 0.14 (April)	2.59 ± 0.28 (October)	1.1 ± 0.08 (October)
Mauna Loa	(24°W, 20°N, 3.40)	125M	SFIT4	4.49 ± 1.8 (April)	1.36 ± 0.31 (April)	2.07 ± 0.43 (August)	0.8 ± 0.04 (August)
La Reunion Maido	(55°E, 21°S, 2.16)	125HR	SFIT4	6.91 ± 2.45 (November)	1.46 ± 0.17 (October)	2.56 ± 0.48 (May)	1.0 ± 0.1 (April)
Lauder	(170°E, 45°S, 0.37)	120HR	SFIT4	5.29 ± 1.18 (November)	1.28 ± 0.19 (October)	1.94 ± 0.28 (July)	0.89 ± 0.09 (February)
Arrival Heights	(167°E, 78°S, 0.2)	120HR	SFIT4	3.22 ± 0.51 (February)	1.0 ± 0.04 (October)	1.78 ± 0.21 (September)	0.67 ± 0.03 (April)

3.1 Seasonal variation

The monthly means of the tropospheric CO and HCN columns at the twelve FTIR stations are shown in Fig. 3. As commonly observed at Hefei (32°N), three monthly mean peaks are evident for tropospheric HCN and CO columns. The magnitude of the tropospheric HCN peak at Hefei (32°N) in May > September > December, while for tropospheric CO column, the magnitude of the peak at Hefei (32°N) in February > September > December. Note that the largest seasonal peak of HCN occurs in May which is 3 months later than that of CO which occurs in February, but the other two seasonal peaks for both species occur in the same months, i.e., in September and December respectively. Otherwise, their seasonal cycles show similarities.

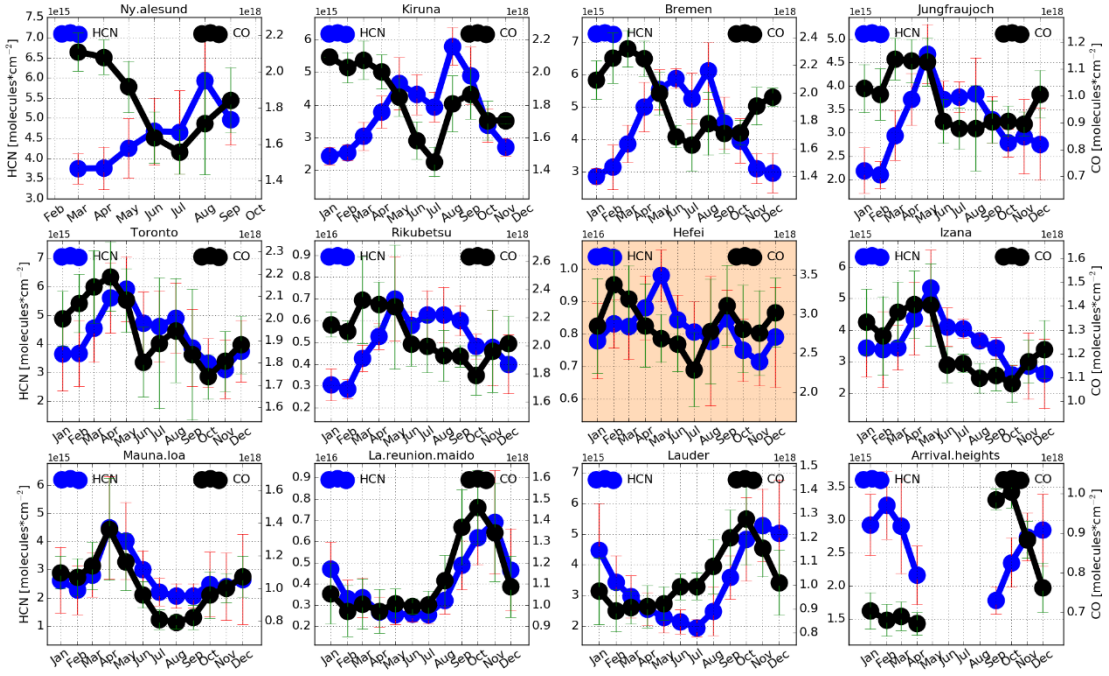

Fig. 3. Monthly means of the tropospheric CO and HCN columns at Ny Alesund, Kiruna, Bremen, Jungfraufoch, Toronto, Rikubetsu, Hefei, Izana, Mauna Loa, La Reunion Maido, Lauder, and Arrival Heights from 2015 to 2018. Vertical error bars represent 1σ within that month. All stations are organised as a function of decreasing latitude.

The tropospheric HCN and CO columns at Hefei (32°N) are higher than the NDACC FTIR observations (see Fig. S2). The tropospheric HCN column reached a maximum of (9.8 ± 0.78) × 10^{15} molecules/cm^2 in May and a minimum of (7.16 ± 0.75) × 10^{15} molecules/cm^2 in November. The tropospheric CO column reached a maximum of (3.38 ± 0.43) × 10^{18} molecules/cm^2 in February and a minimum of (2.29 ± 0.48) × 10^{18} molecules/cm^2 in July (Table 4). In comparison, the seasonal maxima and minima of tropospheric HCN columns at the selected NDACC FTIR stations varied over (3.22 ± 0.51) to (7.0 ± 1.92) × 10^{15} molecules/cm^2 and (1.78 ± 0.21) to (3.75 ± 0.37) × 10^{15} molecules/cm^2, respectively. The seasonal maxima and minima of tropospheric CO columns at the selected NDACC FTIR stations varied over (1.0 ± 0.04) to (2.32 ± 0.31) × 10^{18} molecules/cm^2 and (0.67 ± 0.03) to (1.79 ± 0.14) × 10^{18} molecules/cm^2, respectively (Table 4).

In the northern hemisphere, the phase of the seasonal maxima for tropospheric HCN columns

generally occur in spring or summer, and for CO occur in winter or spring. While in the southern hemisphere, the phase of the seasonal maxima for both tropospheric HCN and CO columns occur in autumn or winter.

3.2 Interannual variability and enhancement

In order to study the interannual variability of HCN and CO, fractional differences in the tropospheric HCN and CO columns relative to their seasonal mean values represented by the cosine fitting at the twelve FTIR stations are shown in Fig.4 and Fig.5, respectively. Enhancements of both tropospheric HCN and CO columns between September 2015 and July 2016 at Hefei (32°N) were observed compared to the same period of measurements in other years. For HCN, the magnitude of the enhancement ranges from 5 to 46% with an average of 26%. The significant enhancements occurred in December 2015 and May 2016 with peaks of 46% and 38%, respectively. By contrast, the magnitude of the enhancement in tropospheric CO column at Hefei (32°N) between September 2015 and July 2016 ranges from 4 to 59% with an average of 27%.The tropospheric CO columns were elevated over its seasonal means by more than 20% from March to April 2016. In addition, an enhancement magnitude of more than 40% were occasionally observed in August and September for both HCN and CO at Hefei (32°N).

The enhancements of both tropospheric HCN and CO columns within the same period were also observed at the selected NDACC stations except Ny Alesund (79°N) and Kiruna (68°N). The winter enhancements were not shown over Ny Alesund (79°N) and Kiruna (68°N) because of the polar night in the Arctic which interrupted the observations in winter. The magnitude of the enhancement in tropospheric HCN column at the selected NDACC stations between September 2015 and July 2016 ranges from 3 to 213%, and for CO ranges from 4 to 62%.

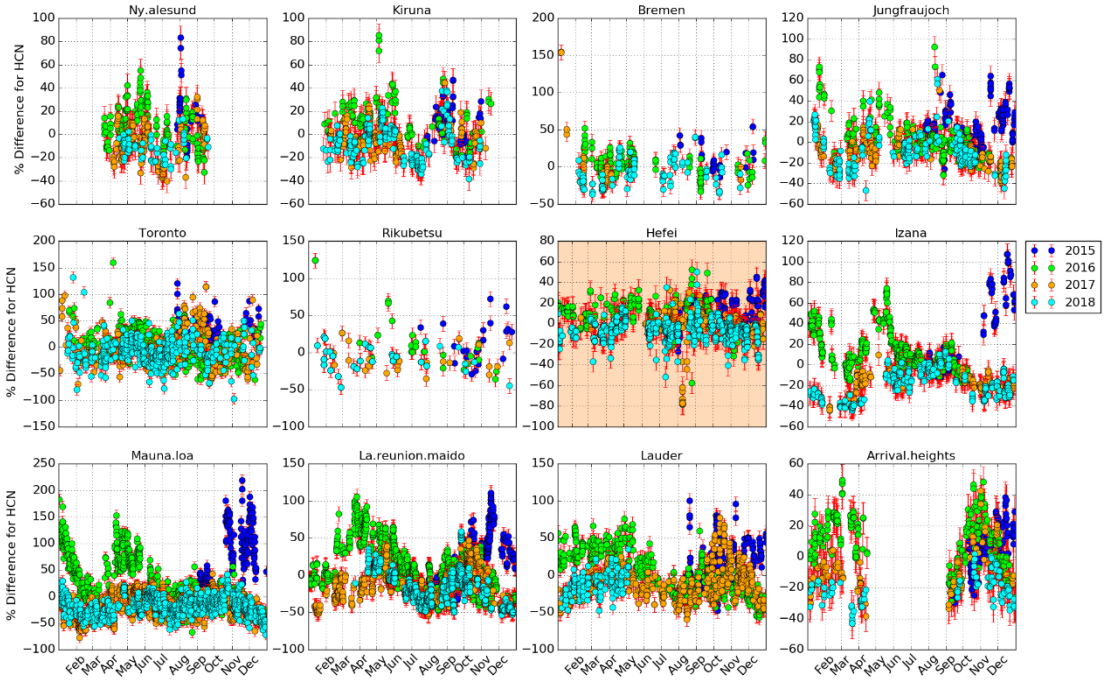

Fig.4. Fractional difference in the partial columns (surface - 15 km) of HCN from 2015 to 2018 at Ny Alesund, Kiruna, Bremen, Jungfraufoch, Toronto, Rikubetsu, Hefei, Izana, Mauna Loa, La Reunion Maido, Lauder, and Arrival Heights relative to their seasonal mean values. Vertical error bars represent the estimated retrieval errors. All stations are organised as a function of decreasing latitude.

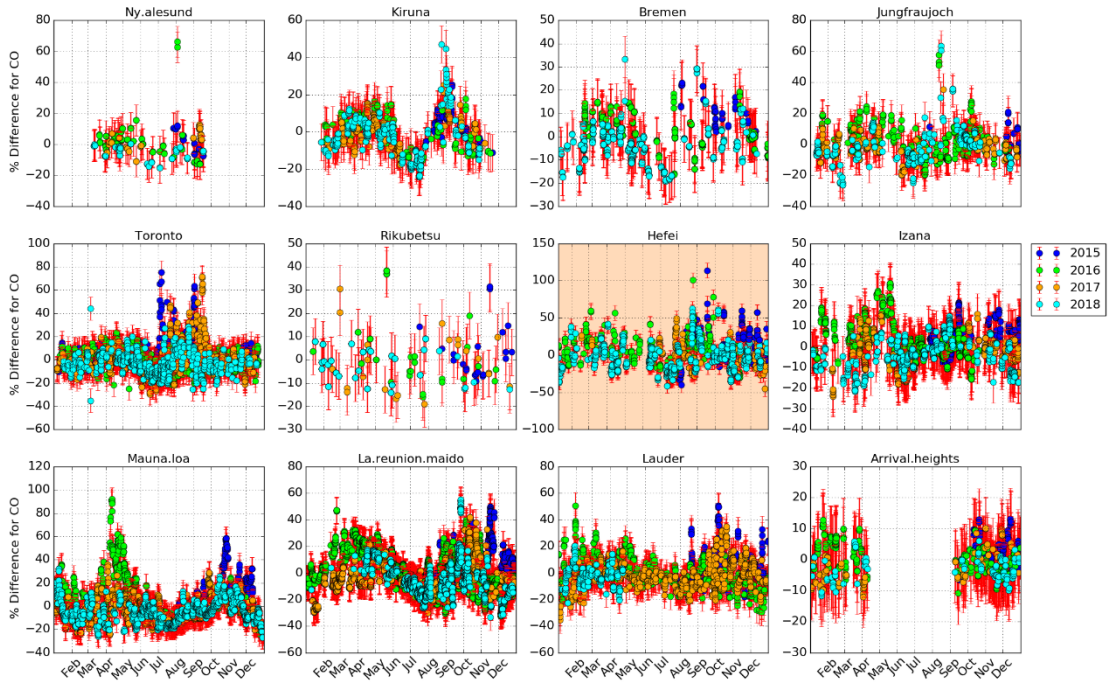

Fig.5. The same as Fig.4 but for CO.

3.3 Correlation with CO and enhancement ratios

The tropospheric HCN columns at the twelve FTIR stations from 2015 to 2018 have been plotted against the coincident CO partial columns (Fig.6). In Fig.7, the correlations between the tropospheric HCN and CO columns at Hefei (32°N) for all spectra recorded throughout the year (gray dots) and those recorded within the selected periods (green dots) are compared. We followed the least squares procedure of York et al., 2004 to fit the coincident measurements using a linear regression, and incorporated the errors in both ordinal and abscissa coordinates into the uncertainty estimation.

Biomass burning is the dominant source of HCN and industrial emissions only contribute additional minor sources (Bange and Williams, 2000; Holzinger et al., 1999; Lobert et al., 1990). In contrast, anthropogenic, biomass burning, CH_4 and NMVOC oxidations are major sources of CO, and their contributions are season and location dependent. Therefore, the correlation between HCN and CO tropospheric column is also season and site dependent. High correlation of these two species is supposed to be observed if biomass burning dominates the CO variability, and vice visa. For the period of 2015 to 2018 in this study, moderate overall correlations between HCN and CO tropospheric columns were present at Jungfraujoch (47°N) and Rikubetsu (43°N), and negative overall correlations were present at Ny Alesund (79°N), Kiruna (68°N), Bremen (53°N), and Arrival Heights (78°S). However, high correlation of these two species were seen at Toronto (44°N), Hefei (32°N), Izana (28°N), Mauna Loa (20°N), La Reunion Maido (21°S), and Lauder (45°S) throughout the year probably because the portion of the fire-affected seasonal measurements at these stations are larger than those at other stations (Fig.6). For the measurements at Hefei (32°N), the high correlations between HCN and CO tropospheric columns deduced from the measurements without March and April (R=0.67, Fig.7 (a)), in May (R=0.69, Fig.7 (b)), in September(R=0.77, Fig.7 (c)), and in December (R=0.65, Fig.7 (d)) are consistent with that deduced from all measurements (R=0.70) (Table 5). However, the correlation slope for the May, September, and December tropospheric columns differ from the annual one, indicating different biomass burning sources in different periods.

For fire-affected measurements, the slope $\Delta HCN/\Delta CO$ defined as enhancement ratio ($EnhR_{HCN}$) is an effective quantity to identify biomass burning emissions (Holzinger et al., 1999; Lutsch et al., 2016; Rinsland et al., 2002; Viatte et al., 2015; Vigouroux et al., 2012; Zhao et al., 2000). Depending on the burnt biomaterials, fire type, the phase of the fire, and the travel time of the plumes, the reported $EnhR_{HCN}$ varied by 2 orders of magnitude. The mean $EnhR_{HCN}$ of 1.34×10^{-3} at Hefei (32°N) falls between the wide range of the HCN/CO ratios measured in laboratory ($0.4 - 7.1\times10^{-3}$ in the work of (Yokelson et al., 1997) and $0.4 - 2.6\times10^{-3}$ in the work of (Holzinger et al., 1999), and $0.94 - 7.4\times10^{-3}$ in the NDACC FTIR measurements (Fig. 6). The mean $EnhR_{HCN}$ at Hefei (32°N) is close

to that at Rikubetsu (43°N) indicating that these two Asian stations share similar biomass burning sources throughout the year. The mean $EnhR_{HCN}$ at Hefei (32°N) is lower than those measured at Jungfraujoch (47°N), Toronto (44°N), Izana (28°N), Mauna Loa (20°N), Lauder (45°S), and La Reunion Maido (21°S) because the emissions of crop residue burning which dominates the HCN enhancements at Hefei (32°N) is lower than those of the boreal or tropical forest burning, which account for the HCN enhancements at aforementioned NDACC stations (Akagi et al., 2011; Akagi et al., 2012; Rinsland et al., 2007; Vigouroux et al., 2012). On the other hand, the Hefei (32°N) site is located in the densely populated part of China, therefore emissions of fossil fuel combustion such as automobile exhaust and industrial processes could elevate the CO background level and hence lessen the $EnhR_{HCN}$.

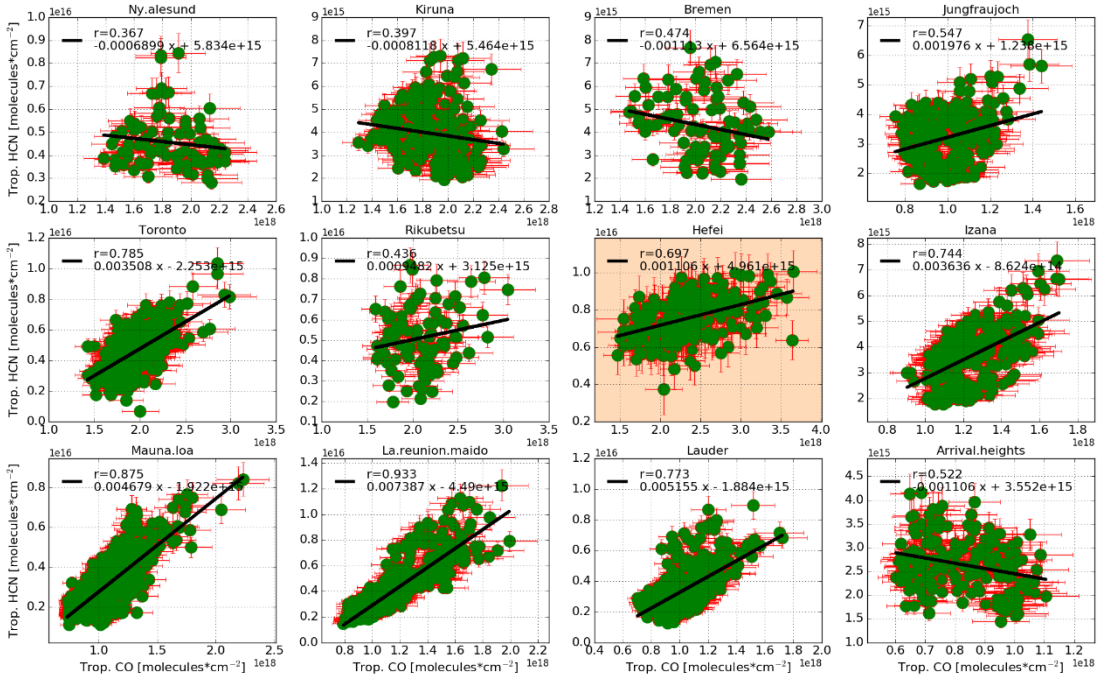

Fig. 6. Correlation plots of daily mean partial columns (surface - 15 km) of HCN versus CO (molecules/cm^2). The linear equation of the fit and the resulting correlation coefficient *r* are shown. The black line is a linear least-squares fit of respective data. All stations are organised as a function of decreasing latitude. Error bars represent the retrieval uncertainties.

Table 5. Correlation between HCN and CO tropospheric columns within each selected period at Hefei (32°N), China. *N* is the number of points, *R* is the correlation coefficient and $EnhR_{HCN}$ is the enhancement ratio.

Gas	Period	without March and April	May	September	December	Mean
HCN	*N*	239	26	56	35	-
	R	0.67	0.69	0.77	0.65	0.7
	EnhR×10^{-3}	1.06	1.48	1.29	1.52	1.34

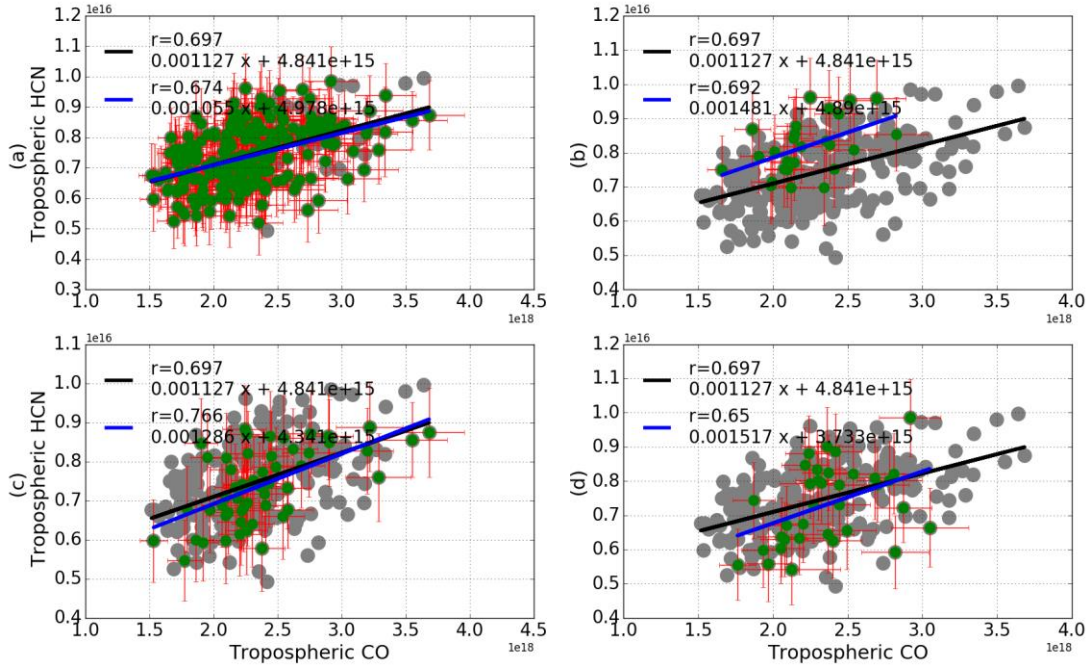

Fig. 7. Correlation plots of daily mean tropospheric columns of HCN versus CO (molecules/cm^2) at Hefei (32°N). The gray dots represent all measurements and the green dots represent the measurements within the selected period: (a) measurements without March and April; (b) measurements in May; (c) measurements in September; (d) measurements in December. The linear equation of the fit and the resulting correlation coefficient *r* are shown. The black line is a linear least-squares fit of the gray data and the blue line is for the green data. Error bars represent the retrieval uncertainties.

4 Source attribution

In order to determine what drives the seasonality and interannual variability of tropospheric HCN in eastern China, it is necessary to match the observed time series with actual biomass burning events, and show that the generated plumes are capable of travelling to the observation site. We did this by using various independent data sets.

1. The 1-hourly instantaneous CO VMR (volume mixing ratio) profiles of the tracers listed in Table 3 provided by a GEOS-Chem tagged CO simulation performed as described in Section 2.2.

2. The global fire atlas data archived by the Fire Information for Resource Management System (FIRMS) which generates fire information from NASA's Moderate Resolution Imaging Spectroradiometer (MODIS) and NASA's Visible Infrared Imaging Radiometer Suite (VIIRS) (https://firms.modaps.eosdis.nasa.gov/download/, last access on 23 May 2019). We have only taken the fire number with a retrieval confidence value of larger than 60% into account.

3. Three dimensional kinematic back trajectories at designated elevations calculated by the Air Resources Laboratory (ARL, http://ready.arl.noaa.gov/HYSPLIT.php, last accessed on 23 May 2019) Hybrid Single Particle Lagrangian Integrated Trajectory (HYSPLIT) model using Global Data Assimilation System (GDAS) meteorological fields (https://ready.arl.noaa.gov/gdas1.php, last accessed on 23 May 2019).

4. The PSCF values calculated by MeteoInfo as described in Section 2.3 using HYSPLIT back trajectories (http://meteothink.org/index.html, last accessed on 17 December 2019).

4.1 Attribution for the seasonality

The GEOS-Chem tagged CO simulation provides a means of evaluating the contribution of CO from anthropogenic, biomass burning and oxidation sources to the measured CO columns at Hefei (32°N). Source attribution is performed as follows. First, the GEOS-Chem CO VMR profiles of all tracers in the grid box containing the Hefei (32°N) site were converted to partial column profiles and linearly interpolated and regridded onto the FTIR vertical retrieval grid. This was necessary in order to account for the differences in the vertical levels of the model and the FTIR (Barret et al., 2003). Then, The GEOS-Chem CO partial column profiles are smoothed by the normalized FTIR CO total column averaging kernel following Rodgers and Connor (2003). The GEOS-Chem CO profiles, FTIR CO profiles and total column averaging kernels are daily averaged and the daily averaged GEOS-Chem profiles are subsequently smoothed. Fig.8 shows the daily-averaged GEOS-Chem and FTIR CO tropospheric columns (surface-15 km) for the simulation

period from 2015 - 2018. The relative contribution of anthropogenic, biomass burning and oxidation tracers are also shown. The GEOS-Chem and FTIR CO tropospheric columns are in good agreement.

The combination of the anthropogenic source and the oxidations of CH_4 and NMVOCs is the greatest contribution to the tropospheric CO column at Hefei (32°N). The magnitude of this combination source varies over 80 to 95% throughout the year. In contrast, the magnitude of biomass burning source varies over 5 to 20%. As shown in Fig.9, the anthropogenic, biomass burning and oxidation sources are all seasonal dependent due to the magnitude of the emissions and the influence of seasonally variable transport. The onset of the anthropogenic contribution begins in July with a maximum in December. In contrast to the anthropogenic influence, the onset of the oxidation contribution begins in January with a maximum in July, as a result of maximum NMVOC emissions in Summer (Sun et al., 2018b). For biomass burning contribution, two onsets were observed. One begins in January with a maximum in April and the other one begins in July with a maximum in October.

After normalizing each biomass burning tracer listed in Table 3 to the total biomass burning contribution, the normalized relative contribution of each individual biomass burning tracer to the total biomass burning associated CO tropospheric column was obtained in Fig.10. The results show that the seasonal maxima in May is largely due to the influence of SEAS biomass burning (41 ± 13.1%). Moderate contributions from EUBA (21 ± 9.3%) and AF (22 ± 4.7%), and small contributions from SA (7.8 ± 2.9%), OCE (1.5 ± 0.8%), and NA (7.7 ± 1.9%) are also observed. The seasonal maxima in September is largely due to the influence of EUBA (38 ± 11.3%) and AF (26 ± 6.7%) biomass burnings. Remaining contributions are from SA (5.1 ± 2.7%), SEAS (14 ± 3.3%), OCE (8.9 ± 7.4%), and NA (13.8 ± 8.4%). For the seasonal maxima in December, contributions from AF, SA, SEAS, EUBA, OCE, and NA are 36 ± 7.1%, 11 ± 1.9%, 11 ± 3.6%, 21 ± 5.2%, 4.8 ± 2.7%, and 18.7 ± 5.2%, respectively.

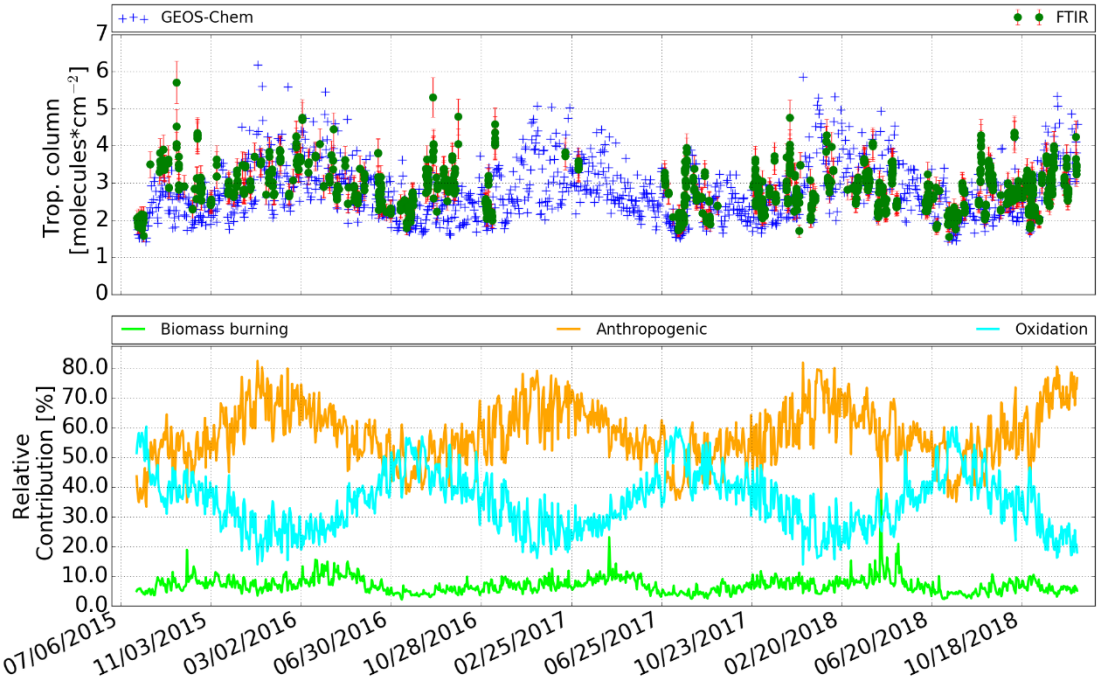

Fig. 8. Daily-mean CO tropospheric column time series of FTIR and GEOS-Chem (top panel) from 2015-2018 at Hefei (32°N). The bottom panel shows the relative contribution (%) of the anthropogenic, biomass burning, and oxidation tracers in the GEOS-Chem simulation to the total CO tropospheric column.

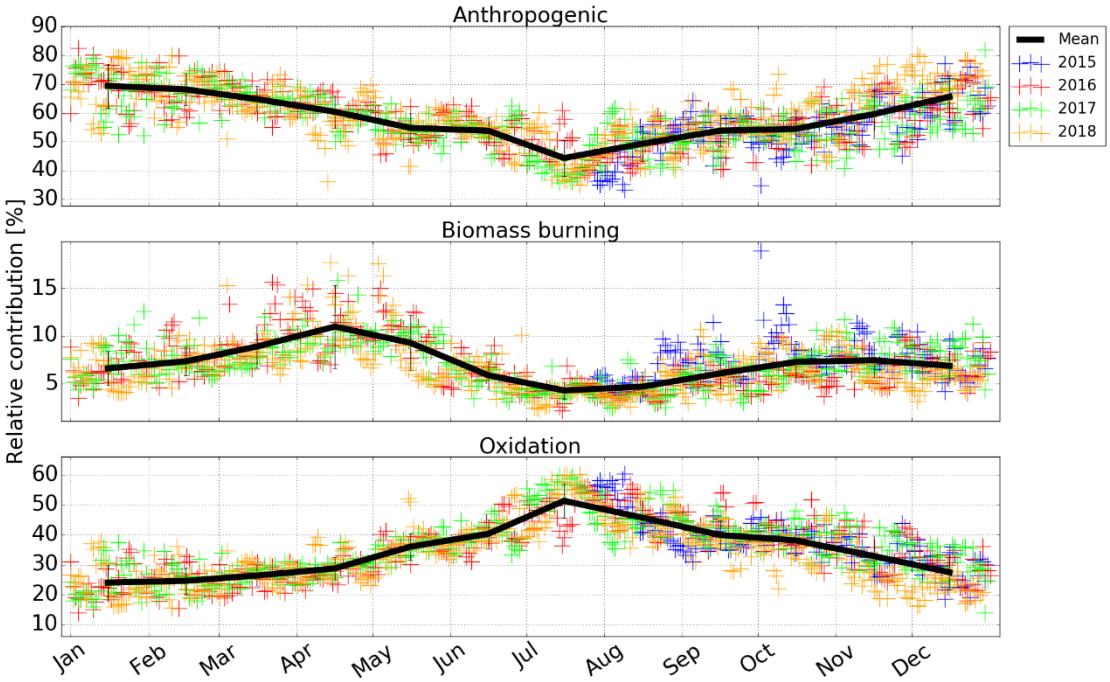

Fig. 9. Seasonality of the relative contribution (%) of the anthropogenic, biomass burning, and oxidation tracers in the GEOS-Chem simulation to the total CO tropospheric column.

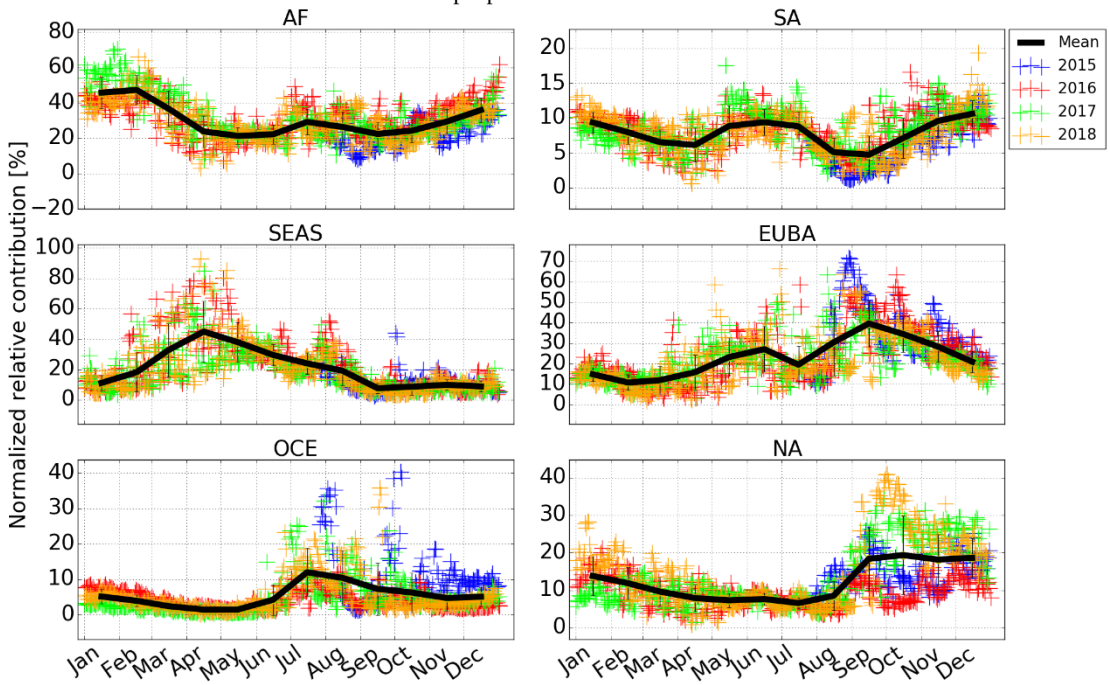

Fig. 10. Seasonality of the normalized relative contribution (%) of the AF, SA, SEAS, EUBA, OCE, and NA biomass burning tracers in the GEOS-Chem simulation to the total biomass burning associated CO tropospheric column.

4.2 Attribution for transport pathway

For each seasonal enhancement of the tropospheric HCN, transport pathway is determined as follows. First, the GEOS-Chem tagged CO simulation is used to calculate the relative contribution of each biomass burning tracer (Fig. 10). For the tracer with a high contribution, the FIRMS global fire map is used to search for potential fire events occurring before the phase of tropospheric HCN enhancement within a one month period. Then, we generated an ensemble of HYSPLIT back trajectories with different travel times and arrival altitudes to judge whether these plumes are capable of travelling to the observation site. For example, for each intensive biomass burning event detected at a specific period, we generated ten back trajectories at different arrival altitudes ranging from 1.5 to 12 km, and modified the end time of these back-trajectories within one day of the observed enhancement. If the back-trajectories intersect a region where the FIRMS fire data

indicates an intensive fire event and the travel duration is within a reasonable range, then this specific fire event could contribute to the observed enhancements at Hefei (32°N) in eastern China. The transport pathway for this enhancement is finally determined.

Fig. 11 demonstrates travel trajectories of the plumes occurred in AF, SEAS & OCE, EUBA, and NA that reached Hefei (32°N) through long range transport. Fig. 12 shows the PSCFs calculated using 13-day HYSPLIT back trajectories that are coincident with the FTIR measurement time. The eastern China, South Asia, Central Asia, Eastern Europe, and Northern Africa had high PSCF weight values in both the first and the second half of the year. The large areas of Southeastern Asian countries including Philippines, Malaysia, and Indonesia, and the Eastern North America were the additional regions with potentially high PSCF weight values in the second half of the year. Generally, trajectories with the same travel time in the second half of the year are longer than those in the first half year, resulting in broader areas with potentially high PSCF weight values.

As shown in Figs.13 and 14, the seasonal biomass burning typically occurs in July – September in southern Africa and in November – February in central Africa. These AF emissions can be transported to eastern China along with the southwestern wind which contributed 25 – 45% of the tropospheric HCN in these periods. The seasonal biomass burning typically occurs in March – May and July – November in central Europe, and in June – September in Siberia. These EUBA emissions can be transported to eastern China along with the northwestern or northern wind which contributed 27 – 40% of the tropospheric HCN in these periods. The seasonal biomass burning typically occurs in March – May in India and South Asia peninsula. Driven by the Asian monsoon anticyclone (AMA), the dominant circulation feature in the Indian–Asian upper troposphere–lower stratosphere region during the Asian monsoon, these emissions can be transported to eastern China which contributed to the tropospheric HCN peak in May. The seasonal biomass burning typically occurs in March – May, July – September, and November – December in the eastern part of China. All these emissions can be transported to the observation site at Hefei (32°N) under favorable meteorological conditions and thus contribute to all the seasonal tropospheric HCN peaks. The SEAS contribution (mainly China, India and South Asia peninsula) varies over 25 to 80% in March to August.

Additionally, a small to moderate portion of wildfire events in central SA, eastern NA, and Northern OCE in autumn or winter could transport to the observation site through large-scale atmospheric circulation, which contributed 5 – 20% of the tropospheric HCN in these periods.

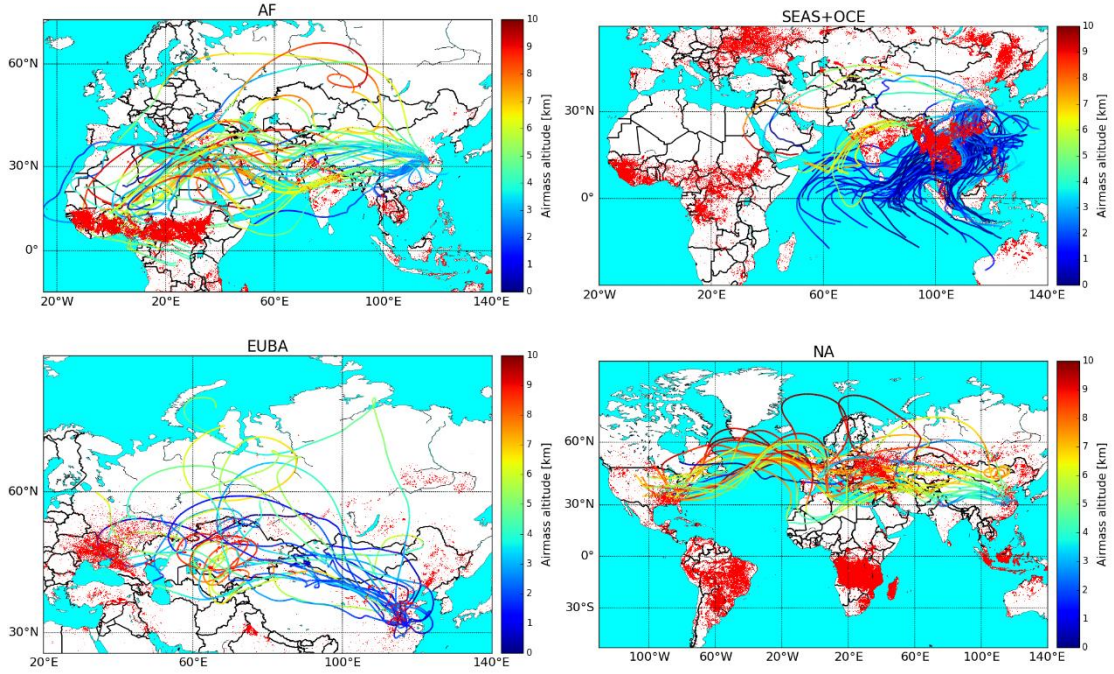

Fig.11. Travel trajectories of the plumes occurred in AF, SEAS & OCE, EUBA, and NA that reached Hefei (32°N) through long range transport. Travel times are 13, 7, 10, and 14 days, respectively. For clarity, only few trajectories are selected for demonstration.

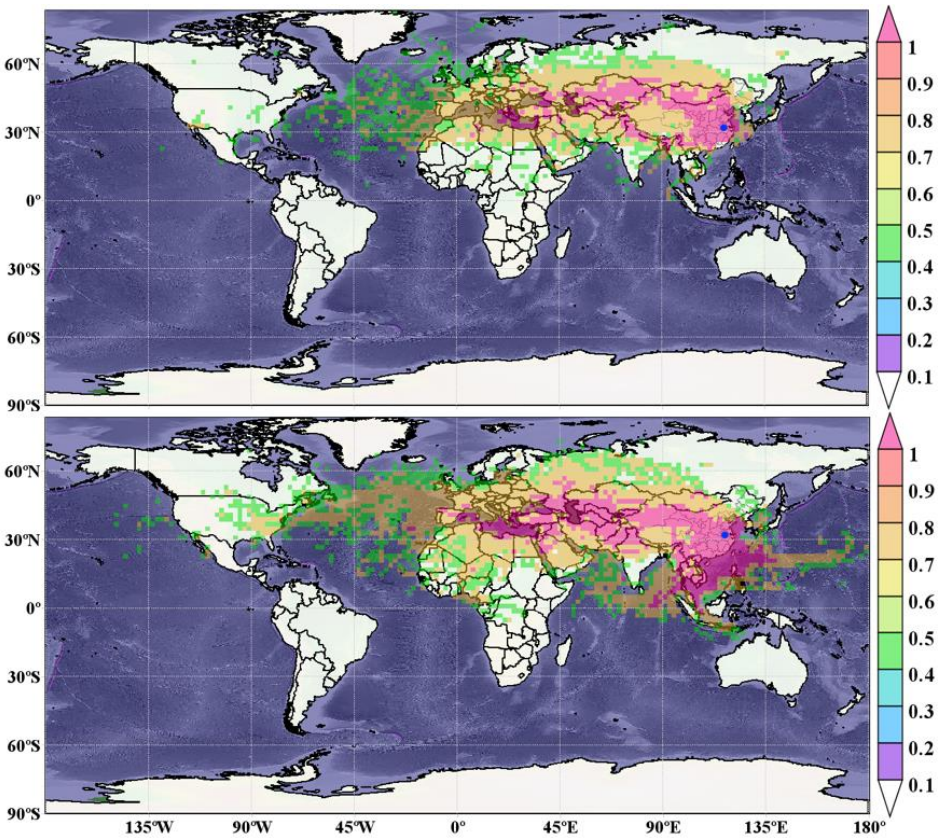

Fig.12. Likely source areas of air mass associated with higher HCN concentrations at Hefei (32°N) in the first half year (top panel) and the second half year (bottom panel) identified using PSCF.

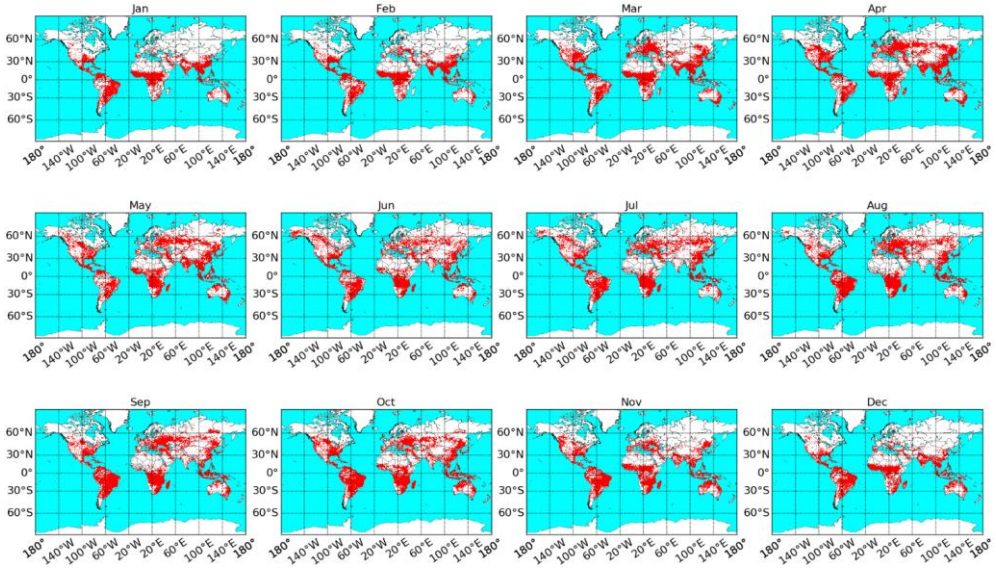

Fig. 13. Global fire map in January to December 2015 accumulated from the FIRMS fire atlas.

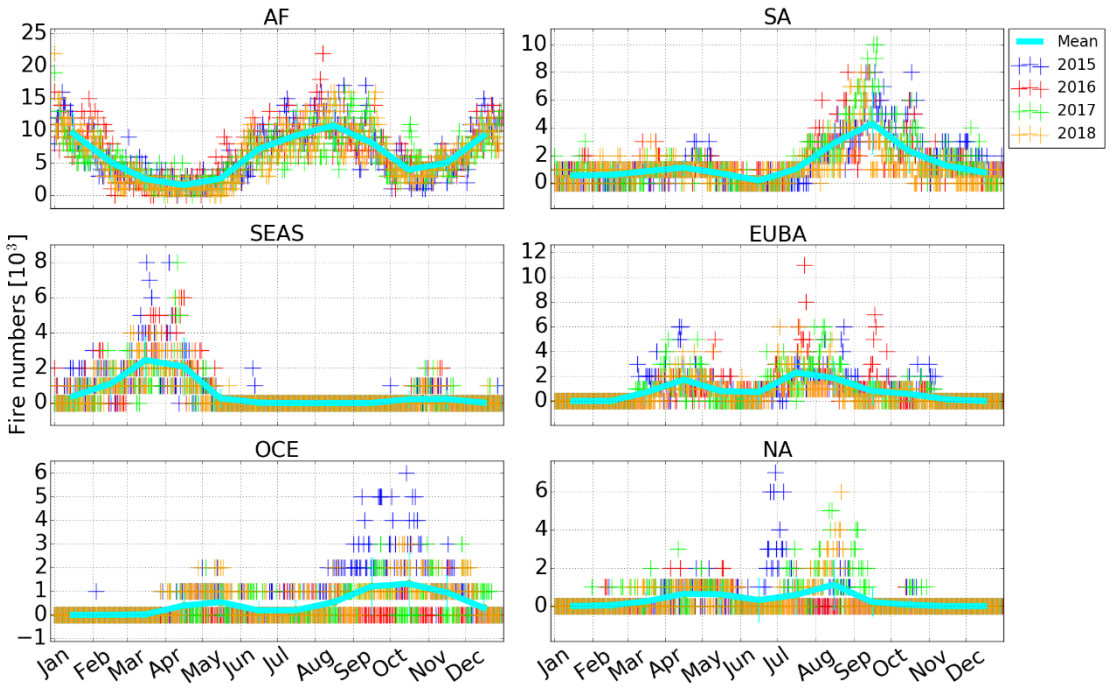

Fig.14. Seasonality of total fire numbers within the AF, SA, SEAS, EUBA, OCE, and NA tracers. All data are accumulated from the FIRMS fire atlas.

4.3 Attribution for interannual variability

In Fig. 9, the biomass burning contribution was elevated by 5 – 15% between September 2015 and July 2016, while no elevations were observed for anthropogenic and oxidation influence. As a result, enhancements of both tropospheric HCN and CO columns between September 2015 and July 2016 at Hefei (32°N) were attributed to an elevated influence of biomass burning. In Fig.10, the relative contribution (%) of the SEAS, EUBA, and OCE biomass burning tracers to the total biomass burning associated CO tropospheric column were elevated by 5 – 20%, 8 – 27%, 8 – 31%, respectively, in the second half of 2015 compared to the same period in other years. The relative contribution (%) of the SEAS and OCE biomass burning tracers to the total biomass burning associated CO tropospheric column were elevated by 8 – 39% and 2 – 7%, respectively, in the first half of 2016 compared to the same period in other years.

The statistical results of the FIRMS fire atlas data in Fig.14 show that, the fire numbers in the SEAS, EUBA, and OCE regions elevated by 21.89%, 15.72%, and 32.68% between September 2015 and July 2016 compared to the same period in other years. These elevated fire numbers in EUBA, SEAS and OCE drove the enhancements of tropospheric HCN and CO columns between September 2015 and July 2016 at Hefei (32°N). In particular, the number of fires in OCE in the second half of 2015 was greatly elevated in comparison with the other years, acting as a dominant source of tropospheric HCN enhancement in September – December 2015. The fire numbers elevated significantly in the SEAS region in the first half of 2016, which dominated the tropospheric HCN enhancement in January – July 2016.

Many studies have revealed that the El Niño Southern Oscillation (ENSO) can cause large scale variations in the convection, circulation, and air temperature of the global atmosphere-ocean system (Liu et al., 2017; Zhao et al., 2002), which could affect the distribution, frequency, and intensity of biomass burning emissions (Schaefer et al., 2018). Furthermore, ENSO could also alter the destruction processes of tropospheric species through their photochemical reactions with tropospheric OH (Zhao et al., 2002). Zhao et al. (2002) found that the abnormally enhancement of tropospheric CO and HCN observed in northern Japan in 1998 were associated with the 1997–1998 ENSO events (Zhao et al., 2002). There is a close correlation between ENSO and HCN columns at Lauder (45°S) (Zeng et al., 2012; Schaefer et al., 2018), and Schaefer et al. (2018) quantified a detectable ENSO influence on biomass burning of up to 51-55% (Schaefer et al., 2018; Zeng et al., 2012). Very likely, the elevated fire number which caused significant enhancements between September 2015 and July 2016 for tropospheric CO and HCN columns at Hefei and most selected NDACC stations were related to the 2015 – 2016 ENSO events.

Compared to the northwestern part of China such as the Xinjiang province and the Tibet plateau, the densely populated eastern parts of China are more suitable for crop planting because of fertile soil and adequate water resources. Historically, Chinese farmers burned their crop residue (such as rice, corn, and wheat straws) after harvest to fertilize the soil for the coming farming season. Post-harvest crop residue is a fine fuel that burns directly in the field and mostly by flaming in many mechanized agricultural systems. In contrast, when crops are harvested by hand the residue is often burned in large piles that may smolder for weeks.

This seasonal crop residue burning season typically occurs in the spring and summer seasons and also occasionally occurs in the autumn and winter. Pollution gases, dust, and suspended particle matters resulting from crop residue burning emissions result in poor air quality that threaten human health and terrestrial ecosystems. The Chinese presidential decree included the prohibition of crop residue burning into the Law of the People's Republic of China on the Prevention and Control of Atmospheric Pollution in August 2015 (http://www.chinalaw.gov.cn, last access on 17 July 2019), and since then the crop residue burning events were banned throughout China. Therefore, we obtain a decrease in fire numbers in China since 2015.

6 Conclusion

The first multiyear measurements of HCN in the polluted troposphere in densely populated eastern China have been presented. Tropospheric HCN columns were derived from solar spectra recorded with ground-based high spectral resolution Fourier transform infrared (FTIR) spectrometer at Hefei (117°10′E, 31°54′N) between 2015 and 2018. The seasonality and interannual variability of tropospheric HCN columns in eastern China have been investigated. The potential sources that drive the observed HCN seasonality and interannual variability were determined by using the GEOS-Chem tagged CO simulation, the global fire maps and the PSCFs (Potential Source Contribution Function) calculated using HYSPLIT back trajectories.

The tropospheric HCN columns over eastern China showed significant seasonal variations with three monthly mean peaks throughout the year. The magnitude of the tropospheric HCN peak in May > September > December. The tropospheric HCN column reached a maximum monthly mean of $(9.8 \pm 0.78) \times 10^{15}$ molecules/cm^2 in May and a minimum monthly mean of $(7.16 \pm 0.75) \times 10^{15}$ molecules/cm^2 in November. In most cases, the tropospheric HCN columns at Hefei (32°N) are higher than the NDACC FTIR observations. Enhancements of the tropospheric HCN columns were observed between September 2015 and July 2016 compared to the same period of measurements in other years. The magnitude of the enhancement ranges from 5 to 46% with an average of 22%. Enhancement of tropospheric HCN (ΔHCN) is correlated with the coincident enhancement of tropospheric CO (ΔCO), indicating that enhancements of tropospheric CO and HCN were due to the same sources.

The GEOS-Chem tagged CO simulation, the global fire maps and the PSCFs analysis revealed that the seasonal maxima in May is largely due to the influence of biomass burning in South Eastern Asia (SEAS) (41 ± 13.1%), Europe and Boreal Asia (EUBA) (21 ± 9.3%) and Africa (AF) (22 ± 4.7%). The seasonal maxima in September is largely due to the influence of biomass burnings in EUBA (38 ± 11.3%), AF (26 ± 6.7%), SEAS (14 ± 3.3%) and NA (13.8 ± 8.4%). For the seasonal maxima in December, dominant contributions are from AF (36 ± 7.1%), EUBA (21 ± 5.2%), and NA (18.7 ± 5.2%).

The enhancements of both tropospheric HCN and CO columns between September 2015 and July 2016 at Hefei (32°N) were attributed to an elevated influence of biomass burnings in SEAS, EUBA, and Oceania (OCE) in this period. In particular, an elevated fire numbers in OCE in the second half of 2015 dominated the tropospheric HCN enhancement in September – December 2015. An elevated fire numbers in SEAS in the first half of 2016 dominated the tropospheric HCN enhancement in January – July 2016.

Most high resolution FTIR instruments are located in Europe and Northern America, whereas the number of sites in Asia, Africa, and South America is very sparse. As one of few FTIR stations on Asian continent, the long-term observations of trace gases at Hefei are crucial to understand global warming, regional pollution, long term transport, and contribute to the evaluation of satellite data and model simulations.

Data availability. The CO and HCN measurements at the selected NDACC sites can be found by the link http://www.ndaccdemo.org, and the CO and HCN measurements at Hefei are available on request.

Author contributions. YS conceived the concept and prepared the paper with inputs from all coauthors. CL, WW, CS, HY, XX, MZ, and JL carried out the experiments. The rest authors contributed to this work via provide refined data or constructive comments.

Competing interests. The authors declare that they have no conflict of interest.

Acknowledgements. This work is jointly supported by the National High Technology Research and Development Program of China (No.2019YFC0214802, No.2017YFC0210002, No. 2016YFC0203302, 2018YFC0213201, 2019YFC0214702, 2016YFC0200404), the National Science Foundation of China (No. 41877309, No.41775025, No. 41575021, No. 51778596, No. 91544212, No. 41722501, No. 51778596), the Sino-German Mobility programme (M-0036), and Outstanding Youth Science Foundation (No. 41722501). The processing and post processing environment for SFIT4 are provided by National Center for Atmospheric Research (NCAR), Boulder, Colorado, USA. The NDACC network is acknowledged for supplying the SFIT software and the HCN and CO data. The LINEFIT code is provided by Frank Hase, Karlsruhe Institute of Technology (KIT), Institute for Meteorology and Climate Research (IMK-ASF), Germany. The MeteoInfo software is provided by Prof. Yaqiang Wang, Chinese Academy of Meteorological Sciences. The authors acknowledge the NOAA Air Resources Laboratory (ARL) for making the HYSPLIT transport and dispersion model available on the Internet. The Mauna Loa (20°N) FTIR site is operated by National Center for Atmospheric Research (NCAR), U.S.A., and the Lauder (45°S) and Arrival Heights (78°S) sites are operated by National Institute of Water & Atmospheric Research, New Zealand. The multi-decadal monitoring program of ULiege at the Jungfraujoch station has been primarily supported by the F.R.S.-FNRS and BELSPO (both in Brussels, Belgium) and by the GAW-CH programme of MeteoSwiss. The International Foundation High Altitude Research Stations Jungfraujoch and Gornergrat (HFSJG, Bern) supported the facilities needed to perform the FTIR observations.

References

Akagi, S. K., Craven, J. S., Taylor, J. W., McMeeking, G. R., Yokelson, R. J., Burling, I. R., Urbanski, S. P., Wold, C. E., Seinfeld, J. H., Coe, H., Alvarado, M. J., and Weise, D. R.: Evolution of trace gases and particles emitted by a chaparral fire in California, Atmospheric Chemistry and Physics, 12, 1397-1421,doi:10.5194/acp-12-1397-2012, 2012.

Ashbaugh, L. L., Malm, W. C., and Sadeh, W. Z.: A residence time probability analysis of sulfur concentrations at Grand Canyon National Park, Atmos. Environ., 19, 1263–1270, 1985.

Akagi, S. K., Yokelson, R. J., Wiedinmyer, C., Alvarado, M. J., Reid, J. S., Karl, T., Crounse, J. D., and Wennberg, P. O.: Emission factors for open and domestic biomass burning for use in atmospheric models, Atmospheric Chemistry and Physics, 11, 4039-4072,doi:10.5194/acp-11-4039-2011, 2011.

Andreae, M. O. and Merlet, P.: Emission of trace gases and aerosols from biomass burning, Global Biogeochemical Cycles, 15, 955-966,doi:Doi 10.1029/2000gb001382, 2001.

Bange, H. W. and Williams, J.: New Directions: Acetonitrile in atmospheric and biogeochemical cycles, Atmospheric Environment, 34, 4959-4960,doi:10.1016/s1352-2310(00)00364-2, 2000.

Bertschi, I., Yokelson, R. J., Ward, D. E., Babbitt, R. E., Susott, R. A., Goode, J. G., and Hao, W. M.: Trace gas and particle emissions from fires in large diameter and belowground biomass fuels, Journal of Geophysical Research-Atmospheres, 108,doi:10.1029/2002jd002100, 2003.

Barret, B., Mazière, M. D., and Mahieu, E.: Ground-based FTIR measurements of CO from the Jungfraujoch: characterisation and comparison with in situ surface and MOPITT data, Atmospheric Chemistry and Physics, 3, 2217–2223, https://doi.org/10.5194/acp-3-2217-2003, 2003.

Chan, K. L.: Biomass burning sources and their contributions to the local air quality in Hong Kong, Science of the Total Environment, 596, 212-221,doi:10.1016/j.scitotenv.2017.04.091, 2017.

Chan, K. L., Wiegner, M., Wenig, M., and Poehler, D.: Observations of tropospheric aerosols and NO_2 in Hong Kong over 5 years using ground based MAX-DOAS, Science of the Total Environment, 619, 1545-1556,doi:10.1016/j.scitotenv.2017.10.153, 2018.

Dimitriou, K. and Kassomenos, P.: Three year study of tropospheric ozone with back trajectories at a metropolitan and a medium scale urban area in Greece, Sci. Total Environ., 502, 493–501, 2015.

De Maziere, M., Thompson, A. M., Kurylo, M. J., Wild, J. D., Bernhard, G., Blumenstock, T., Braathen, G. O., Hannigan, J. W., Lambert, J. C., Leblanc, T., Mcgee, T. J., Nedoluha, G., Petropavlovskikh, I., Seckmeyer, G., Simon, P. C., Steinbrecht, W., and Strahan, S. E.: The Network for the Detection of Atmospheric Composition Change (NDACC): history, status and perspectives, Atmospheric Chemistry and Physics, 18, 4935-4964,doi:10.5194/acp-18-4935-2018, 2018.

Freitas, S. R., Longo, K. M., Chatfield, R., Latham, D., Silva Dias, M. A. F., Andreae, M. O., Prins, E., Santos, J. C., Gielow, R., and Carvalho, Jr, J. A.: Including the sub-grid scale plume rise of vegetation fires in low resolution atmospheric transport models, Atmospheric Chemistry and

Physics, 7, 3385–3398, 2007.
Fisher, J. A., Murray, L., Jones, D. B. A., and Deutscher, N. M.: Improved method for linear carbon monoxide simulation and source attribution in atmospheric chemistry models illustrated using GEOS-Chem v9, Geophysical Model Development, 10, 4129–4144, https://doi.org/10.5194/gmd-10-4129-2017, 2017.
Giglio, L., Randerson, J. T., and van der Werf, G. R.: Analysis of daily, monthly, and annual burned area using the fourth-generation global fire emissions database (GFED4), Journal of Geophysical Research: Biogeosciences, 118, 317–328, https://doi.org/10.1002/jgrg.20042, 2013.
Guenther, A. B., Jiang, X., Heald, C. L., Sakulyanontvittaya, T., Duhl, T., Emmons, L. K., and Wang, X.: The Model of Emissions of Gases and Aerosols from Nature version 2.1 (MEGAN2.1): An extended and updated framework for modeling biogenic emissions, Geoscientific Model Development, 5, 1471–1492, https://doi.org/10.5194/gmd-5-1471-2012, 2012.
Giuseppe, F. D., Rémy, S., Pappenberger, F., and Wetterhall, F.: Using the Fire Weather Index (FWI) to improve the estimation of fire emissions from fire radiative power (FRP) observations, Atmospheric Chemistry and Physics, 18, 5359–5370, https://doi.org/10.5194/acp-18-5359-2018, 2018.
Hase, F., Hannigan, J. W., Coffey, M. T., Goldman, A., Höpfner, M., Jones, N. B., Rinsland, C. P., and Wood, S. W.: Intercomparison of retrieval codes used for the analysis of high-resolution, ground-based FTIR measurements, J. Quant. Spectrosc. Ra., 87, 25–52, 2004.
Hase, F.: Improved instrumental line shape monitoring for the ground-based, high-resolution FTIR spectrometers of the Network for the Detection of Atmospheric Composition Change, Atmospheric Measurement Techniques, 5, 603-610,doi:10.5194/amt-5-603-2012, 2012.
Holzinger, R., Warneke, C., Hansel, A., Jordan, A., Lindinger, W., Scharffe, D. H., Schade, G., and Crutzen, P. J.: Biomass burning as a source of formaldehyde, acetaldehyde, methanol, acetone, acetonitrile, and hydrogen cyanide, Geophysical Research Letters, 26, 1161-1164,doi:10.1029/1999gl900156, 1999.
Holtslag, A. A. M. and Boville, B. A.: Local Versus Nonlocal Boundary-Layer Diffusion in a Global Climate Model, Journal of Climate, 6, 1825–1842, https://doi.org/10.1175/1520-0442(1993)006<1825:LVNBLD>2.0.CO;2, 1993.
Kaiser, J. W., Heil, A., Andreae, M. O., Benedetti, A., Chubarova, N., Jones, L., Morcrette, J.-J., Razinger, M., Schultz, M. G., Suttie, M.,and van der Werf, G. R.: Biomass burning emissions estimated with a global fire assimilation system based on observed fire radiative power, Biogeosciences, 9, 527–554, https://doi.org/10.5194/bg-9-527-2012, 2012.
Kaiser, A., Scheifinger, H., Spangl,W.,Weiss, A., Gilge, S., Fricke, W., Ries, L., Cemas, D., and Jesenovec, B.: Transport of nitrogen oxides, carbon monoxide and ozone to the alpine global atmosphere watch stations Jungfraujoch (Switzerland), Zugspitze and Hohenpeißenberg (Germany), Sonnblick (Austria) and Mt.Krvavec (Slovenia), Atmos. Environ., 41, 9273–9287, 2007.
Hoesly R. M., Smith S. J., Feng L. Y., Klimont Z., Janssens-Maenhout G., Pitkanen T., Seibert J. J., Vu L., Andres R. J., Bolt R. M., Bond T. C., Dawidowski L., Kholod N., Kurokawa J., Li M., Liu L., Lu Z. F., Moura M. C. P., O'Rourke P. R., and Zhang Q., "Historical (1750-2014) anthropogenic emissions of reactive gases and aerosols from the Community Emissions Data System (CEDS)," Geosci. Model Dev. 11, 369-408 (2018).
Li, Q., Palmer, P. I., Pumphrey, H. C., Bernath, P., and Mahieu, E.: What drives the observed variability of HCN in the troposphere and lower stratosphere?, Atmospheric Chemistry and Physics, 9, 8531-8543,doi:10.5194/acp-9-8531-2009, 2009.
Li, Q. B., Jacob, D. J., Bey, I., Yantosca, R. M., Zhao, Y. J., Kondo, Y., and Notholt, J.: Atmospheric hydrogen cyanide (HCN): Biomass burning source, ocean sink?, Geophysical Research Letters, 27, 357-360,doi:Doi 10.1029/1999gl010935, 2000.
Li, Q. B., Jacob, D. J., Yantosca, R. M., Heald, C. L., Singh, H. B., Koike, M., Zhao, Y. J., Sachse, G. W., and Streets, D. G.: A global three-dimensional model analysis of the atmospheric budgets of HCN and CH3CN: Constraints from aircraft and ground measurements, Journal of Geophysical Research-Atmospheres, 108,doi:Artn 882710.1029/2002jd003075, 2003.
Li M., Zhang Q., Kurokawa J., Woo J. H., He K. B., Lu Z. F., Ohara T., Song Y., Streets D. G., Carmichael G. R., Cheng Y. F., Hong C. P., Huo H., Jiang X. J., Kang S. C., Liu F., Su H., and Zheng B., "MIX: a mosaic Asian anthropogenic emission inventory under the international collaboration framework of the MICS-Asia and HTAP," Atmos Chem Phys 17, 935-963 (2017).
Liu, Y., Cobb, K. M., Song, H. M., Li, Q., Li, C. Y., Nakatsuka, T., An, Z. S., Zhou, W. J., Cai, Q. F., Li, J. B., Leavitt, S. W., Sun, C. F., Mei, R. C., Shen, C. C., Chan, M. H., Sun, J. Y., Yan, L. B., Lei, Y., Ma, Y. Y., Li, X. X., Chen, D. L., and Linderholm, H. W.: Recent enhancement of central Pacific El Nino variability relative to last eight centuries, Nature Communications,8,doi:ARTN 1538610.1038/ncomms15386, 2017.

Lobert, J. M., Scharffe, D. H., Hao, W. M., and Crutzen, P. J.: Importance of biomass burning in the atmospheric budgets of nitrogen-containing gases, Nature, 346, 552-554,doi:10.1038/346552a0, 1990.

Lupu, A., Kaminski, J. W., Neary, L., McConnell, J. C., Toyota, K., Rinsland, C. P., Bernath, P. F., Walker, K. A., Boone, C. D., Nagahama, Y., and Suzuki, K.: Hydrogen cyanide in the upper troposphere: GEM-AQ simulation and comparison with ACE-FTS observations, Atmospheric Chemistry and Physics, 9, 4301-4313,doi:10.5194/acp-9-4301-2009, 2009.

Lutsch, E., Dammers, E., Conway, S., and Strong, K.: Long-range transport of NH_3, CO, HCN, and C_2H_6 from the 2014 Canadian Wildfires, Geophysical Research Letters, 43, 8286-8297,doi:10.1002/2016gl070114, 2016.

Lutsch, E., Strong, K., Jones, D. B. A., Blumenstock, T., Conway, S., Fisher, J. A., Hannigan, J. W., Hase, F., Kasai, Y., Mahieu, E., Makarova, M., Morino, I., Nagahama, T., Notholt, J., Ortega, I., Palm, M., Poberovskii, A. V., Sussmann, R., and Warneke, T.: Detection and Attribution of Wildfire Pollution in the Arctic and Northern Mid-latitudes using a Network of FTIR Spectrometers and GEOS-Chem, Atmos. Chem. Phys. Discuss., https://doi.org/10.5194/acp-2019-881, in review, 2019.

Mahieu, E., Zander, R., Delbouille, L., Demoulin, P., Roland, G., and Servais, C.: Observed trends in total vertical column abundances of atmospheric gases from IR solar spectra recorded at the Jungfraujoch, Journal of Atmospheric Chemistry, 28, 227-243,doi:10.1023/a:1005854926740, 1997.

Nagahama, Y. and Suzuki, K.: The influence of forest fires on CO, HCN, C_2H_6, and C_2H_2 over northern Japan measured by infrared solar spectroscopy, Atmospheric Environment, 41, 9570-9579,doi:10.1016/j.atmosenv.2007.08.043, 2007.

Notholt, J., Toon, G. C., Rinsland, C. P., Pougatchev, N. S., Jones, N. B., Connor, B. J., Weller, R., Gautrois, M., and Schrems, O.: Latitudinal variations of trace gas concentrations in the free troposphere measured by solar absorption spectroscopy during a ship cruise, Journal of Geophysical Research-Atmospheres, 105, 1337-1349,doi:10.1029/1999jd900940, 2000.

Patra, P. K., Houweling, S., Krol, M., Bousquet, P., Belikov, D., Bergmann, D., Bian, H., Cameron-Smith, P., Chipperfield, M. P., Corbin,K., Fortems-Cheiney, A., Fraser, A., Gloor, E., Hess, P., Ito, A., Kawa, S. R., Law, R. M., Loh, Z., Maksyutov, S., Meng, L., Palmer,P. I., Prinn, R. G., Rigby, M., Saito, R., and Wilson, C.: TransCom model simulations of CH4 and related species: Linking transport,surface flux and chemical loss with CH4 variability in the troposphere and lower stratosphere, Atmospheric Chemistry and Physics, 11,12 813–12 837, https://doi.org/10.5194/acp-11-12813-2011, 2011.

Polissar, A., Hopke, P., Paatero, P., Kaufmann, Y., Hall, D., Bodhaine, B., Dutton, E., and Harris, J.: The aerosol at Barrow, Alaska: long-term trends and source locations, Atmos. Environ., 33, 2441–2458, 1999.

Rinsland, C. P., Dufour, G., Boone, C. D., Bernath, P. F., Chiou, L., Coheur, P. F., Turquety, S., and Clerbaux, C.: Satellite boreal measurements over Alaska and Canada during June-July 2004: Simultaneous measurements of upper tropospheric CO, C_2H_6, HCN, CH_3Cl, CH_4, C_2H_2, CH_3OH, HCOOH, OCS, and SF_6 mixing ratios, Global Biogeochemical Cycles, 21,doi:Artn Gb3008 10.1029/2006gb002795, 2007.

Rinsland, C. P., Jones, N. B., Connor, B. J., Wood, S. W., Goldman, A., Stephen, T. M., Murcray, F. J., Chiou, L. S., Zander, R., and Mahieu, E.: Multiyear infrared solar spectroscopic measurements of HCN, CO, C_2H_6,and C_2H_2 tropospheric columns above Lauder, New Zealand (45 degrees S latitude), Journal of Geophysical Research-Atmospheres, 107,doi:Artn 418510.1029/2001jd001150, 2002.

Rodgers, C. D.: Inverse Methods for Atmospheric Sounding: Theory and Practice, Singapore, 2000.

Rodgers, C. D. and Connor, B. J.: Intercomparison of remote sounding instruments, Journal of Geophysical Research: Atmospheres, 108,4116, https://doi.org/10.1029/2002JD002299, 2003.

Rothman, L. S., Gordon, I. E., Barbe, A., Benner, D. C., Bernath, P. E., Birk, M., Boudon, V., Brown, L. R., Campargue, A., Champion, J. P., Chance, K., Coudert, L. H., Dana, V., Devi, V. M., Fally, S., Flaud, J. M., Gamache, R. R., Goldman, A., Jacquemart, D., Kleiner, I., Lacome, N., Lafferty, W. J., Mandin, J. Y., Massie, S. T., Mikhailenko, S. N., Miller, C. E., Moazzen-Ahmadi, N., Naumenko, O. V., Nikitin, A. V., Orphal, J., Perevalov, V. I., Perrin, A., Predoi-Cross, A., Rinsland, C. P., Rotger, M., Simeckova, M., Smith, M. A. H., Sung, K., Tashkun, S. A., Tennyson, J., Toth, R. A., Vandaele, A. C., and Vander Auwera, J.: The HITRAN 2008 molecular spectroscopic database, Journal of Quantitative Spectroscopy & Radiative Transfer, 110, 533-572,doi:10.1016/j.jqsrt.2009.02.013, 2009.

Rémy, S., Veira, A., Paugam, R., Sofiev, M., Kaiser, J. W., Marenco, F., Burton, S. P., Benedetti, A., Engelen, R. J., Ferrare, R., and Hair, J. W.: Two global data sets of daily fire emission injection heights since 2003, Atmospheric Chemistry and Physics, 17, 2921–2942, https://doi.org/10.5194/acp-17-2921-2017, 2017.

Spivakovsky, C. M., Logan, J. A., Montzka, S. A., Balkanski, Y. J., Foreman-Fowler, M., Jones, D. B. A., Horowitz, L. W., Fusco, A. C.,Brenninkmeijer, C. A. M., Prather, M. J.,Wofsy, S. C., and McElroy, M. B.: Three-dimensional climatological distribution of tropospheric OH: Update and evaluation, Journal of Geophysical Research: Atmospheres, 105, 8931–8980, https://doi.org/10.1029/1999JD901006, 2000.

Sofiev, M., Ermakova, T., and Vankevich, R.: Evaluation of the smoke-injection height from wild-land fires using remote-sensing data, Atmospheric Chemistry and Physics, 12, 1995–2006, https://doi.org/10.5194/acp-12-1995-2012, 2012.

Shindell, D. T., Faluvegi, G., Stevenson, D. S., Krol, M. C., Emmons, L. K., Lamarque, J.-F., Pétron, G., Dentener, F. J., Ellingsen, K., Schultz, M. G.,Wild, O., Amann,M., Atherton, C. S., Bergmann, D. J., Bey, I., Butler, T., Cofala, J., Collins,W. J., Derwent, R. G., Doherty, R.M., Drevet, J., Eskes, H. J., Fiore, A. M., Gauss, M., Hauglustaine, D. A., Horowitz, L. W., Isaksen, I. S. A., Lawrence, M. G., Montanaro,V., Müller, J.-F., Pitari, G., Prather, M. J., Pyle, J. A., Rast, S., Rodriguez, J. M., Sanderson, M. G., Savage, N. H., Strahan, S. E., Sudo, K., Szopa, S., Unger, N., van Noije, T. P. C., and Zeng, G.: Multimodel simulations of carbon monoxide: Comparison with observations and projected near-future changes, Journal of Geophysical Research: Atmospheres, 111, L01 104, https://doi.org/10.1029/2006JD007100, 2006.

Schaefer, H., Smale, D., Nichol, S. E., Bromley, T. M., Brailsford, G. W., Martin, R. J., Moss, R., Englund Michel, S., and White, J. W. C.: Limited impact of El Niño–Southern Oscillation on variability and growth rate of atmospheric methane, Biogeosciences, 15, 6371-6386,doi:10.5194/bg-15-6371-2018, 2018.

Sun, Y. W., Liu, C., Palm, M., Vigouroux, C., Notholt, J., Hui, Q. H., Jones, N., Wang, W., Su, W. J., Zhang, W. Q., Shan, C. G., Tian, Y., Xu, X. W., De Maziere, M., Zhou, M. Q., and Liu, J. G.: Ozone seasonal evolution and photochemical production regime in the polluted troposphere in eastern China derived from high-resolution Fourier transform spectrometry (FTS) observations, Atmospheric Chemistry and Physics, 18, 14569-14583,doi:10.5194/acp-18-14569-2018, 2018a.

Sun, Y. W., Palm, M., Liu, C., Hase, F., Griffith, D., Weinzierl, C., Petri, C., Wang, W., and Notholt, J.: The influence of instrumental line shape degradation on NDACC gas retrievals: total column and profile, Atmospheric Measurement Techniques, 11, 2879-2896,doi:10.5194/amt-11-2879-2018, 2018b.

Tang, G., Wang, Y., Li, X., Ji, D., Hsu, S., and Gao, X.: Spatial-temporal variations in surface ozone in Northern China as observed during 2009–2010 and possible implications for future air quality control strategies, Atmos. Chem. Phys., 12, 2757-2776,doi:10.5194/acp-12-2757-2012, 2012.

Tian, Y., Sun, Y., Liu, C., Wang, W., Shan, C., Xu, X., and Hu, Q.: Characterisation of methane variability and trends from near-infrared solar spectra over Hefei, China, Atmospheric Environment, 173,doi:10.1016/j.atmosenv.2017.11.001, 2017.

Viatte, C., Strong, K., Hannigan, J., Nussbaumer, E., Emmons, L. K., Conway, S., Paton-Walsh, C., Hartley, J., Benmergui, J., and Lin, J.: Identifying fire plumes in the Arctic with tropospheric FTIR measurements and transport models, Atmospheric Chemistry and Physics, 15, 2227-2246,doi:10.5194/acp-15-2227-2015, 2015.

Viatte, C., Strong, K., Walker, K. A., and Drummond, J. R.: Five years of CO, HCN, C_2H_6, C_2H_2, CH_3OH, HCOOH and H_2CO total columns measured in the Canadian high Arctic, Atmospheric Measurement Techniques, 7, 1547-1570,doi:10.5194/amt-7-1547-2014, 2014.

Vigouroux, C., Stavrakou, T., Whaley, C., Dils, B., Duflot, V., Hermans, C., Kumps, N., Metzger, J. M., Scolas, F., Vanhaelewyn, G., Muller, J. F., Jones, D. B. A., Li, Q., and De Maziere, M.: FTIR time-series of biomass burning products (HCN, C_2H_6, C_2H_2, CH_3OH, and HCOOH) at Reunion Island (21 degrees S, 55 degrees E) and comparisons with model data, Atmospheric Chemistry and Physics, 12, 10367-10385,doi:10.5194/acp-12-10367-2012, 2012.

Wang, T., Xue, L. K., Brimblecombe, P., Lam, Y. F., Li, L., and Zhang, L.: Ozone pollution in China: A review of concentrations, meteorological influences, chemical precursors, and effects, Science of the Total Environment, 575, 1582-1596,doi:10.1016/j.scitotenv.2016.10.081, 2017.

Xiaoyan, W., Huixiang, W., and Shaoli, W.: Ambient formaldehyde and its contributing factor to ozone and OH radical in a rural area, Atmospheric Environment, 44, 2074-2078,doi:https://doi.org/10.1016/j.atmosenv.2010.03.023, 2010.

Xing, C., Liu, C., Wang, S., Chan, K. L., Gao, Y., Huang, X., Su, W., Zhang, C., Dong, Y., Fan, G., Zhang, T., Chen, Z., Hu, Q., Su, H., Xie, Z., and Liu, J.: Observations of the vertical distributions of summertime atmospheric pollutants and the corresponding ozone production in Shanghai, China, Atmos. Chem. Phys., 17, 14275-14289,doi:10.5194/acp-17-14275-2017, 2017.

Yevich, R. and Logan, J. A.: An assessment of biofuel use and burning of agricultural waste in the developing world, Global Biogeochemical Cycles, 17, 1095,

https://doi.org/10.1029/2002GB001952, 2003.
Yokelson, R. J., Susott, R., Ward, D. E., Reardon, J., and Griffith, D. W. T.: Emissions from smoldering combustion of biomass measured by open-path Fourier transform infrared spectroscopy, Journal of Geophysical Research-Atmospheres, 102, 18865-18877,doi:10.1029/97jd00852, 1997.
York, D., Evensen, N. M., Martinez, M. L., and Delgado, J. D.: Unified equations for the slope, intercept, and standard errors of the best straight line, American Journal of Physics, 72, 367-375,doi:10.1119/1.1632486, 2004.
Yin, X., Kang, S., de Foy, B., Cong, Z., Luo, J., Zhang, L., Ma, Y., Zhang, G., Rupakheti, D., and Zhang, Q.: Surface ozone at Nam Co in the inland Tibetan Plateau: variation, synthesis comparison and regional representativeness, Atmos. Chem. Phys., 17, 11293–11311, https://doi.org/10.5194/acp-17-11293-2017, 2017.
Zeng, G., Wood, S. W., Morgenstern, O., Jones, N. B., Robinson, J., and Smale, D.: Trends and variations in CO, C_2H_6, and HCN in the Southern Hemisphere point to the declining anthropogenic emissions of CO and C_2H_6, Atmospheric Chemistry and Physics, 12, 7543-7555,doi:10.5194/acp-12-7543-2012, 2012.
Zhao, Y., Kondo, Y., Murcray, F. J., Liu, X., Koike, M., Irie, H., Strong, K., Suzuki, K., Sera, M., and Ikegami, Y.: Seasonal variations of HCN over northern Japan measured by ground-based infrared solar spectroscopy, Geophysical Research Letters, 27, 2085-2088,doi:Doi 10.1029/1999gl011218, 2000.
Zhao, Y., Strong, K., Kondo, Y., Koike, M., Matsumi, Y., Irie, H., Rinsland, C. P., Jones, N. B., Suzuki, K., Nakajima, H., Nakane, H., and Murata, I.: Spectroscopic measurements of tropospheric CO, C_2H_6, C_2H_2,and HCN in northern Japan, Journal of Geophysical Research-Atmospheres, 107,doi:Artn 434310.1029/2001jd000748, 2002.